

## Research Paper

## Smoothed particle hydrodynamics (SPH) modelling for rainfall-induced unsaturated slope failure considering void ratio dependence and variability

Guodong Ma<sup>a</sup>, Annan Zhou<sup>a,1,\*</sup>, Ha H. Bui<sup>b</sup><sup>a</sup> Department of Civil and Infrastructure Engineering, School of Engineering, Royal Melbourne Institute of Technology (RMIT), Melbourne, Victoria 3001, Australia<sup>b</sup> Department of Civil and Environmental Engineering, Monash University, Clayton, Victoria 3800, Australia

## ARTICLE INFO

## Keywords:

Smoothed particle hydrodynamics (SPH)  
 Rainfall-induced slope failure  
 Unsaturated soil  
 Constitutive model  
 Large deformation  
 Void ratio dependence and variability

## ABSTRACT

Rainfall-induced unsaturated slope failures are among the most frequent and destructive forms of landslides worldwide, often resulting in significant casualties and economic losses. Accurately predicting such failures requires not only a robust numerical approach that captures the coupled hydraulic and mechanical behaviours of unsaturated soils, but also a thorough understanding of how spatial variability of soil properties influences slope stability. In this study, smoothed particle hydrodynamics (SPH) is employed in conjunction with an advanced unsaturated constitutive model to investigate, for the first time, the effects of void ratio dependence and variability on rainfall-induced unsaturated slope failure. The model captures the coupled hydro-mechanical behaviour of unsaturated soils, accounting for the influence of void ratio on water retention, infiltration and strength characteristics. A single-layer multiphase SPH approach is employed, where each particle simultaneously represents the water, air, and solid phases, enabling the efficient and robust simulation of large-deformation problems. The SPH model is applied to a synthetic slope with spatial variable soil properties to explore how heterogeneity in void ratio alters failure mechanisms and onset conditions. The results provide new insights into the role of void ratio heterogeneity in rainfall-triggered landslides and demonstrate the potential of advanced SPH modelling for practical probabilistic analysis in geotechnical applications.

## 1. Introduction

Soil slope failures triggered by rainfall represent one of the most common and extensive forms of destructive landslides worldwide (Ozturk et al., 2022, Amarasinghe et al., 2024, Yang and Zhang, 2024). These events pose serious threats to human lives, cause significant damage to infrastructure and assets, and disrupt natural ecosystems (Baum and Godt, 2010, Yang et al., 2022). In areas with high vulnerability, such events can escalate into a severe disaster. For example, intense rainfall triggered a landslide and flooding in Petrópolis, Brazil, in February 2022, resulting in at least 220 fatalities (Ozturk et al., 2022). Similarly, extremely heavy rainfall caused the collapse of the Meida Highway in Guangdong, China, in May 2024, leading to 48 deaths (Xue et al., 2025). To understand and prevent these kinds of disasters, extensive research has been conducted. The soil slope is initially unsaturated with high suction. Consequently, most studies focus on rainfall-induced failures of unsaturated slopes by examining various contributing factors. These factors can be roughly categorised into three

main groups: (1) hydraulic properties, including parameters of the soil water characteristic curve (Rahimi et al., 2010), permeability coefficient (Rahimi et al., 2010), water content (Tohari et al., 2007), porosity (Zhang et al., 2005, Le et al., 2019); (2) soil strength properties, such as cohesion and friction angle (Feng et al., 2021); and (3) rainfall patterns, including intensity and duration (Rahimi et al., 2011, Yubonchit et al., 2017, Lu et al., 2024).

Various numerical approaches have been employed to simulate the rainfall-induced unsaturated slope failure, including the finite element method (FEM) (Chen et al., 2021, Zhang et al., 2005, Borja and White, 2010); particle finite element method (PFEM) (Jin and Yin, 2022, Yuan et al., 2022); material point method (MPM) (Yerro et al., 2015, Alonso, 2021); smoothed particle hydraulics (SPH) method (Bui and Nguyen, 2021, Lian et al., 2022); finite volume method (FVM) (Showkat et al., 2022) and hybrid approaches such as FEM-MPM (Liu and Wang, 2021, Lu et al., 2024). Among them, FEM is perhaps the most widely used computational method. However, it faces challenges in accurately predicting failures involving large deformations due to mesh distortion.

\* Corresponding author.

E-mail address: [Annan.Zhou@rmit.edu.au](mailto:Annan.Zhou@rmit.edu.au) (A. Zhou).<sup>1</sup> ORCID: 0000-0001-5209-5169

Although PFEM can handle large deformations, it incurs high computational costs due to frequent remeshing. Compared to MPM, SPH is a truly mesh-free method that does not require background meshes and is particularly effective in modelling large deformations (Lian et al., 2022). The SPH method was originally developed for astrophysical applications (Gingold and Monaghan, 1977). Since its first application in geotechnical engineering (Bui et al., 2008), SPH has developed rapidly and been applied to a wide range of geotechnical problems, including granular flows (Bui et al., 2008, Nguyen et al., 2017), slope failures (Pastor et al., 2009, Morikawa and Asai, 2022, Lian et al., 2023), soil–water interactions (Bui et al., 2007, Shao, 2010), seepage flows (Bui and Nguyen, 2017, Peng et al., 2017, Lian et al., 2021), and internal erosion (Ma et al., 2022, Ma et al., 2024). In recent years, fully coupled hydro-mechanical SPH frameworks (Lian et al., 2022, Ma et al., 2022, Morikawa and Asai, 2022, Lian et al., 2023) have been developed. Lian et al., (2022) and Nguyen et al. (2025) demonstrated the capability of this SPH framework in predicting rainfall-induced unsaturated slope failures involving large deformations, with numerical results validated against well-documented experimental and field data. Therefore, this fully coupled SPH framework is well-suited for studying rainfall-induced slope failure.

In addition to the large deformation, heterogeneity is another key point to address the rainfall-induced unsaturated slope failures. Many researchers have employed probabilistic analyses to study rainfall-triggered slope failures (Lu et al., 2020, Le et al., 2019, Liu and Wang, 2021, Lu et al., 2024). For example, Liu and Wang (2021) analysed the process of rainfall-induced landslides using random FEM-MPM by quantifying both landslide probability and consequences. Furthermore, Lu et al. (2024) utilised the FEM-MPM method to evaluate the exceedance probability of run-out distance over a given time period, accounting for uncertainties in both soil properties and rainfall. In current random field applications to slope stability and failure, traditional elasto-plastic models (e.g., Mohr–Coulomb) are typically used, with friction angle and cohesion treated as spatially variable parameters (Griffiths and Fenton, 2004, Cho, 2010, Griffiths et al., 2009, Liu et al., 2017). For slope failures involving seepage flow, it is common to generate a random field for the permeability coefficient (Griffiths and Fenton, 1993, Ng et al., 2022, Robbins et al., 2021, Xiong et al., 2025). However, due to the numerous variables involved, uncertainty is often assigned to the parameters of the soil water characteristic curve (SWCC) (Phoon et al., 2010, Chiu et al., 2012, Wang et al., 2020) rather than to the generation of random fields. It is now well established that the mechanical behaviour of porous media is strongly influenced by porosity. Advanced constitutive models based on critical state soil mechanics introduce state parameters linked to porosity or void ratio, which can capture the different behaviours of dense and loose soils. Andrade et al. (2008) combined a random porosity field with a critical state model for sand and demonstrated that specimen strength is affected by both the degree and orientation of anisotropy in porosity. More recently, Fang et al. (2024) used a hypoplastic critical state-based model to show that increased spatial variability in void ratio can alter slope failure modes.

The evolution of pore water pressure plays a key role in unsaturated slope failure (Wei et al., 2021). Porosity directly influences this process by controlling hydraulic properties such as permeability and saturated water content. Mukhlisin et al. (2006) emphasized that soils with higher effective porosity in the surface layer can store more water, thereby delaying infiltration into deeper layers. Le et al. (2012, 2019) examined unsaturated seepage through random porosity fields in earth embankments and found that porosity heterogeneity significantly influences infiltration patterns, often producing preferential flow zones and uneven pore pressure distributions. While porosity clearly links soil's hydraulic and mechanical properties, few studies have simultaneously addressed its variability in both hydraulic and mechanical aspects. For example, Le et al. (2013) combined porosity and pre-consolidation stress random fields in settlement problems. Masoudian et al. (2019) modelled

multivariate dependent random fields of void ratio, dry unit weight, friction, and cohesion in coupled hydro-mechanical analyses. Building on these insights, the present study aims to systematically investigate the role of void ratio variability on the coupled hydro-mechanical behaviour of slopes by employing a fully coupled smoothed particle hydrodynamics (SPH) framework.

No matter what numerical approaches are adopted, to accurately predict changes in soil strength and deformation during the infiltration process in both unsaturated and saturated slopes, an advanced unsaturated soil constitutive model is essential – particularly the one that can take into account hydro-mechanical coupling and void ratio dependence. Following pioneering work done by Alonso et al. (1990), Zhou et al. (2012a, 2012b) proposed a fully coupled hydro-mechanical unsaturated constitutive model using the effective degree of saturation and Bishop's effective stress. The fully coupled hydro-mechanical unsaturated model proposed by Zhou et al. (2012a, 2012b) has been implemented within FEM (Zhang et al., 2019) to account for both hydraulic and mechanical loading conditions. Zhou and Sheng (2015) further developed this model to incorporate the effects of initial density (i.e. void ratio) on coupled hydro-mechanical behaviours of the soil, such as the dependence of loading–collapse volume on initial void ratio and density effect on the shearing-induced saturation change.

Building on the work of Lian et al. (2022), the present study adopts a single-layer, multiphase, fully coupled hydro-mechanical SPH framework to further study the rainfall-induced unsaturated slope failure involving large deformation. Particularly, in this study, we implement the simplified version of the constitutive model developed by Zhou and Sheng (2015) within a fully coupled SPH numerical framework to investigate how void ratio dependence and variability influence rainfall-induced slope failure mechanisms. This paper is organised as follows: Section 2 introduces the fully coupled hydro-mechanical numerical framework, the governing equations as well as the advanced unsaturated constitutive model. Section 3 presents the basic SPH equations and the SPH approximations of the governing equations. Section 4 discusses the validation and verification of the unsaturated constitutive model, both at the element level and within the SPH numerical framework through the granular collapse and simple shear tests. Section 5 presents the numerical analysis of rainfall-induced unsaturated slope failure, considering the dependence and spatial variability of void ratio. Finally, some useful conclusions have been drawn for practice and future study.

## 2. Hydro-mechanical coupled numerical framework for unsaturated soil

### 2.1. Governing equations

The main governing equations for fully coupled hydro-mechanical simulations in unsaturated soil are summarised as following referred to (Lian et al., 2022, Ma et al., 2022, Ma et al., 2024). Eq. (1) describes the change in porosity resulting from soil deformation. Eq. (2) represents the momentum equation governing the motion of the soil. Eq. (3) is the hydraulic equation used to update the pore water pressure head within the soil.

$$\frac{d\phi}{dt} = (1 - \phi) \nabla \cdot \mathbf{v}_s \quad (1)$$

$$\rho_t \frac{d\mathbf{v}_s}{dt} = \nabla \cdot \boldsymbol{\sigma}_t + \rho_t \mathbf{b} \quad (2)$$

$$\frac{dh}{dt} = \frac{1}{C_{sr}} \left\{ -S_r \nabla \cdot \mathbf{v}_s + \nabla \cdot [k_w \nabla (h + z)] + \frac{1}{g} \nabla \cdot \left( k_w \frac{d\mathbf{v}_s}{dt} \right) \right\} \quad (3)$$

where  $\phi$  is the porosity;  $\mathbf{v}_s$  is velocity vector of soil mixture;  $\rho_t$  is the total density of soil mixture;  $\boldsymbol{\sigma}_t$  is the total stress of the soil mixture;  $\mathbf{b}$  is the body force;  $h$  is the pore water pressure head;  $S_r$  is the degree of saturation;  $k_w$  is the water permeability coefficient;  $z$  is the elevation;  $g$  is the

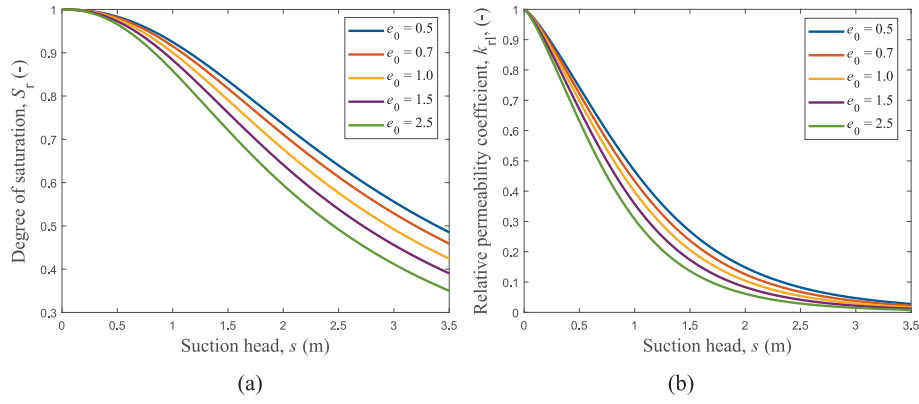


Fig. 1. Degree of saturation and relative permeability coefficient at different values of void ratio.

gravity;  $C_{sr}$  is the storage coefficient,  $C_{sr} = \left( \frac{S_r \phi \gamma_w}{K_w} + \phi \frac{dS_r}{dh} \right)$ ;  $\gamma_w$  is the specific weight of water;  $K_w$  is the water bulk modulus,  $K_w = 2.2$  GPa.

## 2.2. Hydraulic model

In this study, porosity and degree of saturation both influence seepage flow. The permeability coefficient is formulated as follows:

$$k(\phi, S_r) = k_{sat}(\phi) k_{rl}(S_r) \quad (4)$$

The term  $k_{sat}(\phi)$  represents the saturated permeability coefficient, which is defined based on the Kozeny-Carman relationship (Kozeny, 1927) as follows:

$$k_{sat}(\phi) = k_{sat0} \frac{(1 - \phi_0)^2}{\phi_0^3} \frac{\phi^3}{(1 - \phi)^2} \quad (5)$$

where  $k_{sat0}$  is the initial saturated permeability coefficient value;  $\phi$  is the porosity;  $\phi_0$  is the initial porosity. In saturated soils, an increase in porosity generally leads to a higher saturated permeability coefficient.

The term  $k_{rl}(S_r)$  is the relative permeability coefficient in an unsaturated state, describing the change of permeability coefficient related to the degree of saturation in unsaturated soil through the Van Genuchten model (Van Genuchten, 1980).

$$k_{rl}(S_r) = S_e^{g_c} \left[ 1 - (1 - S_e^{-(1/g_c)})^{-g_c} \right]^2 \quad (6)$$

$$S_e = (S_r - S_{res}) / (S_{sat} - S_{res}) \quad (7)$$

where  $S_r$  is the degree of saturation;  $S_e$  is the effective degree of saturation;  $S_{res}$  is the residual degree of saturation, assumed to be 0;  $S_{sat}$  is the degree of saturation at full saturation, assumed to be 1;  $g_1$  and  $g_c$  are empirical fitting parameters.

The relationship between the degree of saturation and the suction head is written as (Van Genuchten, 1980):

$$S_r = S_{res} + (S_{sat} - S_{res}) [1 + (g_a | -h |)^{g_n}]^{-g_c} \quad (8)$$

where  $-h$  is the suction head (m);  $g_a$  and  $g_n$  are fitting parameters;  $g_c = (1 - g_n) / g_n$ .

In the original model of Zhou and Sheng (2015), hydraulic hysteresis is considered. However, in this study, the influence of hydraulic hysteresis is considered negligible, as no wetting-drying cycles are simulated. To facilitate implementation within the SPH framework while accounting for the dependence of degree of saturation on void ratio, we adopt the equation proposed by Gallipoli et al. (2003), instead of the more complex hysteresis-based equations used by Zhou and Sheng (2015). In this study, the parameter  $g_a$  becomes a function of void ratio  $e$  (Gallipoli et al., 2003):

$$g_a = \alpha e^\varphi \quad (9)$$

where  $\alpha$  and  $\varphi$  are constant parameters. Eq. (9) highlights that void-ratio dependence has been incorporated into the soil-water characteristic curve through the parameter  $g_a$ , which is related to the air-entry value.

Using the above Eq. (8) and Eq. (9), the degree of saturation accounts for soil's volume change through void ratio, which has been well validated by experimental data (Gallipoli et al., 2003). Fig. 1 (a) presents the predicted relationships between the degree of saturation and suction head for different void ratios. The chosen soil water characteristic curve (SWCC) parameters including  $S_{res} = 0$ ,  $S_{sat} = 1$ ,  $g_1 = 0$ ,  $g_n = 2.286$ ,  $g_c = -0.563$  are consistent with previous studies (Lian et al., 2021, Galavi, 2010). Parameters controlling void ratio dependence are  $\alpha = 0.5(1/m)$ , and  $\varphi = 0.2$ , with the void ratio ranging from 0.5 to 2.5. The calculated parameters  $g_a = \alpha e^\varphi$  ranges from 0.4 to 0.7, aligning well within the range of values from literature (Lian et al., 2021, Galavi, 2010, Phoon et al., 2010). As observed, an increase in void ratio leads to a decrease in the degree of saturation at a given suction head. The relation between relative permeability coefficient and suction head for different void ratios (equation (6)) is presented in Fig. 1 (b). In the unsaturated state, an increase in void ratio leads to a reduction in the relative permeability coefficient.

It is important to note that SWCC parameter selection significantly influences seepage flow timing and, thus, the onset of wetting-induced unsaturated slope failure. Since this study primarily investigates the influence of spatial variability and void ratio dependence on slope failure, the void ratio and its spatial randomness are treated as variables, while all other SWCC parameters remain fixed.

## 2.3. Constitutive relationship

A simplified concept of effective stress in unsaturated soils is introduced through Bishop's effective stress equation (Bishop, 1959, Sheng et al., 2003, Zhou and Sheng, 2015):

$$\sigma' = \sigma - \mathbf{m} S_e p_w \quad (10)$$

where  $\sigma'$  is the effective stress;  $\sigma$  is the total stress;  $\mathbf{m}$  is the column vector with 1 at normal stress entries and 0 at shear stress entries;  $p_w$  is the pore water pressure; the pore air pressure is neglected. It is noted that the effective degree of saturation  $S_e$  is chosen as the basic constitutive variable, and it can revert to degree of saturation  $S_r$  if appropriate values for  $S_{res}$  and  $S_{sat}$  are selected.

The increment of effective stress increment ( $d\sigma'$ ) is given by Hooke's law:

$$d\sigma' = \mathbf{D}^e : (d\epsilon - d\epsilon^p) \quad (11)$$

where  $d\epsilon$  is the total strain increment;  $d\epsilon^p$  is the plastic strain increment,

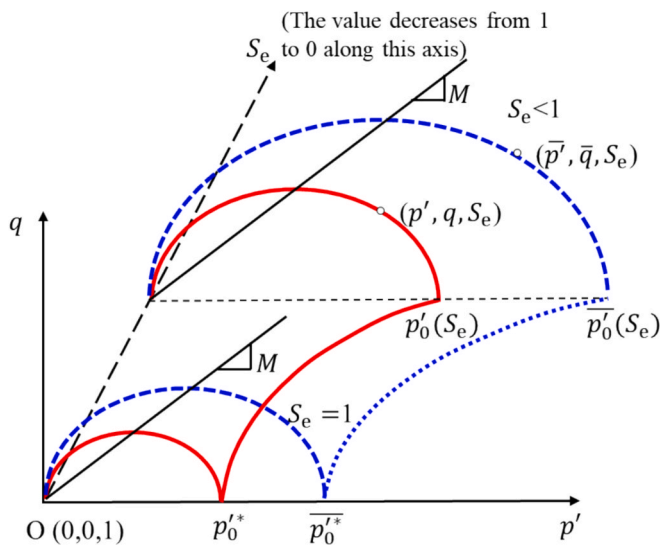


**Fig. 2.** Sub-loading and yield surface of the constitutive model, after [Zhou and Sheng \(2015\)](#).

$\mathbf{D}^e = \left(K - \frac{2}{3}G\right)\boldsymbol{\delta} \otimes \boldsymbol{\delta} + 2GI$  is the elastic stiffness matrix;  $K$  is the elastic bulk modulus and  $G$  is the shear modulus, which are given as follows:

$$K = \frac{(1+e)p'}{\kappa} \quad G = \frac{3(1-2\mu)K}{2(1+\mu)} \quad (12)$$

where  $p'$  is the mean effective stress;  $\kappa$  is the slope of the swelling line;  $\mu$  is the Poisson's ratio.

The incremental plastic strain ( $d\epsilon^p$ ) in Eq. (11) is given as:

$$d\epsilon^p = d\lambda \frac{\partial g(\sigma')}{\partial \sigma'} \quad (13)$$

where  $d\lambda$  is the plastic multiplier, which can be determined by solving consistency condition on the yield surface;  $g(\sigma')$  is the plastic potential function.

The adopted unsaturated constitutive model proposed by [Zhou and Sheng \(2015\)](#) uses sub-loading surface and reference yield surface to describe the initial density effects on soil's strength. The sub-loading surface and reference yield surface are expressed as follows and illustrated in [Fig. 2](#) ([Zhou and Sheng, 2015](#)):

$$f(p', q, p_0(S_e)) = p' + \frac{q^2}{M^2 p'} - p_0(S_e) = 0 \quad (14)$$

$$f(\overline{p}, \overline{q}, \overline{p}_0(S_e)) = \overline{p} + \frac{\overline{q}^2}{M^2 \overline{p}} - \overline{p}_0(S_e) = 0 \quad (15)$$

where  $p'$  is the mean effective stress;  $q$  is the deviatoric stress;  $p'_0(S_e)$  is the pre-consolidation effective stress under certain  $S_e$ ; the over bar '—' means the variables related to the reference yield surface;  $M$  is the critical stress ratio.

The dilatancy rule defining the potential function using associated flow rule presents as follows,

$$d_r = \frac{d\varepsilon_v^p}{d\varepsilon_a^p} = \frac{M^2 p'^2 - q^2}{2p'q} \quad (16)$$

where  $d_r$  is the dilatancy rate;  $d\varepsilon_v^p$  and  $d\varepsilon_q^p$  are plastic volumetric and deviatoric strain increments.

The similarity ratio  $R$  is determined by:

$$R = \frac{p'_0(S_e)}{\overline{p'_0(S_e)}} \quad (17)$$

$R$  reflects the influence of the initial soil density (i.e., the initial void ratio) on the soil's strength. The value of  $R$  ranges from 0 to 1. When  $R < 1$ , the soil is in a dense state, whereas  $R = 1$  represents the loosest state.

To incorporate the effect of suction in unsaturated soils, the pre-consolidation effective stress  $p'_0(s_e)$  at a given suction on sub-loading surface is associated with the load-collapse (LC) yield surface (Alonso et al., 1990, Zhou and Sheng, 2015):

$$p'_0(S_e) = p_c \left( \frac{p_0}{p_c} \right)^{\frac{\lambda_0 - \kappa}{\lambda(S_e) - \kappa}} \quad (18)$$

$$\lambda(S_e) = \lambda_0 - (\lambda_0 - \kappa)(1 - S_e)^{a_1} \quad (19)$$

where  $p_0'^*$  is the pre-consolidation effective stress under fully saturated state;  $p_c = 1$  Pa is the reference effective stress on normal consolidation line (NCL) line in  $e - \ln p'$  plane;  $\lambda(S_e)$  represents the slope value of the NCL line at a certain effective saturation  $S_e$ ;  $\lambda_0$  is the slope value of the normal consolidation line in  $e - \ln p'$  plane under fully saturated condition;  $\kappa$  is the slope of the swelling line in  $e - \ln p'$  plane; and  $a_1$  is constant.

The pre-consolidation effective stress at full saturation state ( $p_0^*$ ) on sub-loading surface is governed by a volumetric hardening law, referred to unified hardening (UH) model (Yao et al., 2009, Yao et al., 2012):

$$dp_0^{rs} = \frac{(1+e)p_0^{rs}}{(\lambda_0 - \kappa)} \Omega d\varepsilon_v^p \quad (20)$$

$$\Omega = \frac{M_f^4 - \eta^4}{M^4 - \eta^4} \quad (21)$$

where  $M_f = 6 \left[ \sqrt{\frac{M_h}{R} \left( 1 + \frac{M_h}{R} \right)} - \frac{M_h}{R} \right]$ ;  $R$  is the similarity ratio;  $M_h = \frac{M^2}{12(3-M)}$ ;  $\eta$  is the stress ratio and equals to  $q/p'$ .

Similarity, the pre-consolidation effective stress  $\bar{p}_0^*(S_e)$  at a given suction on the reference yield surface can be determined, and the hardening law for the pre-consolidation effective stress at the fully saturated state ( $\bar{p}_0^*$ ) on the reference yield surface follows the same form as the modified Cam-clay model (Roscoe et al., 1963, Schofield and Wroth, 1968):

$$\overline{p_0'}(S_e) = p_c \left( \frac{\overline{p_0^{rs}}}{p_c} \right)^{\frac{\lambda_0 - \kappa}{\lambda(S_e) - \kappa}} \quad (22)$$

$$d\overline{p_0^{rk}} = \frac{(1+e)\overline{p_0^{rk}}}{(\lambda_0 - \kappa)} d\varepsilon_v^p \quad (23)$$

The initial stress state ( $p', q$ ) and initial suction ( $s$ ) and initial effective degree of saturation ( $S_{e0}$ ) are commonly known values. Therefore, the initial pre-consolidation effective stress  $p'_0(S_{e0})$  on sub-loading surface is calculated as:

$$p'_0(S_{e0}) = p' + \frac{q^2}{M^2 p'} \quad (24)$$

The initial pre-consolidation effective stress  $\bar{p}_0(s_{e0})$  under initial effective degree of saturation ( $s_{e0}$ ) on reference yield surface is determined following the approach proposed in [Zhou and Sheng \(2015\)](#):

$$\overline{p_0'}(S_{e0}) = \exp\left(\frac{e_{\text{ref}} - e_0 + \lambda(S_{e0})\ln p_c - \kappa \ln p_0'(S_{e0})}{\lambda(S_{e0}) - \kappa}\right) \quad (25)$$



where the  $e_{\text{ref}}$  is the reference void ratio on normal consolidation line (NCL) line when  $p_c = 1$  Pa;  $e_0$  is the initial void ratio of the soil. Eq. (25) demonstrates the dependence of the soil's mechanical behaviour on void ratio, expressed via its relationship with the pre-consolidation effective stress.

In this study, to improve numerical accuracy and stability, the semi-implicit stress integration algorithm proposed by Bui and Nguyen (2021) is adopted for the unsaturated constitutive model. The details of this algorithm are provided in the Appendix.

### 3. SPH integration method

#### 3.1. SPH equations and kernel function

Smoothed particle hydrodynamics (SPH) is a mesh-free numerical method based on continuum mechanics, where the computational domain is discretised into particles. These particles carry key field properties, such as mass, density, and velocity. The enhanced SPH equations for scalar values ( $f(\mathbf{x}_i)$ ), first-order derivatives ( $\nabla_i f(\mathbf{x}_i)$ ), and the Laplacian operator ( $\nabla_i^2 f(\mathbf{x}_i)$ ) are presented (Bui and Nguyen, 2021):

$$f(\mathbf{x}_i) = \sum_{j=1}^N \frac{m_j}{\rho_j} f(\mathbf{x}_j) W_{ij} \quad (26)$$

$$\nabla_i f(\mathbf{x}_i) = \sum_{j=1}^N \frac{m_j}{\rho_j} [f(\mathbf{x}_j) - f(\mathbf{x}_i)] \cdot \hat{\nabla}_i W_{ij} \quad (27)$$

$$\nabla_i^2 f(\mathbf{x}_i) = 2 \sum_{j=1}^N \frac{m_j}{\rho_j} [f(\mathbf{x}_j) - f(\mathbf{x}_i)] \frac{\mathbf{x}_{ji} \cdot \hat{\nabla}_i W_{ij}}{|\mathbf{x}_{ji}|^2} \quad (28)$$

where the subscripts  $i$  and  $j$  refer to the quantity evaluated at the position of particle  $i$  and  $j$ , respectively;  $\rho_j$  and  $m_j$  are the density and mass of particle  $j$ , respectively;  $N$  is the total number of neighbouring particles located within the support domain of particle  $i$ ;  $\mathbf{x}_{ji}$  is the relative distance between two particles, defined by  $\mathbf{x}_{ji} = \mathbf{x}_j - \mathbf{x}_i$ ;  $W_{ij}$  and  $\nabla_i W_{ij}$  are the kernel function and its gradient;  $\hat{\nabla}_i W_{ij} = L_{ij} \nabla_i W_{ij}$  and  $L_{ij} = \left[ \sum_{j=1}^N \frac{m_j}{\rho_j} (\mathbf{x}_j - \mathbf{x}_i) \nabla_i W_{ij} \right]^{-1}$  is renormalization matrix.

Instead of using Eq. (28), following SPH approximations is used in this study to further improve the accuracy when particles' positions are disordered (Lian et al., 2021, Lian et al., 2022):

$$\frac{\partial^2 f(\mathbf{x}_i)}{\partial x^m \partial x^n} = \sum_{j=1}^N V_j (f(\mathbf{x}_j) - f(\mathbf{x}_i)) \mathcal{S}^{mn} \tilde{F}_{ij} - \frac{\partial f(\mathbf{x}_i)}{\partial x_j^m} \sum_{j=1}^N V_j x_{ji}^n \mathcal{S}^{mn} \tilde{F}_{ij} \quad (29)$$

where  $V_j$  is the volume occupied by the particle  $j$ ;  $\mathcal{S}^{mn} = 4 \frac{x_{ji}^m x_{ji}^n}{|\mathbf{x}_{ji}|^2} - \delta^{mn}$ ;

$\tilde{F}_{ij} = \frac{x_{ji}^m}{|\mathbf{x}_{ji}|^2} \cdot \hat{\nabla}_i^m W_{ij}$ ;  $\hat{\nabla}_i^m W_{ij} = L_{ij}^{mn} \nabla_i^m W_{ij}$ ; the renormalisation matrix  $L_{ij}^{mn}$

is written as  $L_{ij}^{mn} = \left[ \sum_{j=1}^N \frac{m_j}{\rho_j} (x_j - x_i)^m \nabla_i^n W_{ij} \right]^{-1}$ .

In this study, the cubic spline kernel function is employed:

$$W(q, h_{\text{sml}}) = \alpha_d \begin{cases} \frac{2}{3} - q^2 + \frac{1}{2} q^3 (0 \leq q < 1) \\ \frac{1}{6} (2 - q)^3 (1 \leq q < 2) \\ 0 (q \geq 2) \end{cases} \quad (30)$$

where  $\alpha_d$  is the dimensional normalising factor,  $\alpha_d = 15/7\pi h^2$  in two-dimension;  $q = |\mathbf{x}_{ij}|/h_{\text{sml}}$  is the normalised distance between particles;  $h_{\text{sml}}$  is the smooth length of the kernel function, which is chosen as 1.2 times the initial particle distance; the SPH compact support domain is  $2h_{\text{sml}}$ .

#### 3.2. SPH approximations of governing equations

The porosity equation for the soil mixture is approximated as follows:

$$\left( \frac{d\phi}{dt} \right)_i = (1 - \phi_i) \sum_{j=1}^N \frac{m_{ij}}{\rho_{ij}} (\mathbf{v}_{sj} - \mathbf{v}_{si}) \cdot \hat{\nabla}_i W_{ij} \quad (31)$$

where  $\phi_i$  is the porosity of particle  $i$ ;  $\mathbf{v}_{si}$  and  $\mathbf{v}_{sj}$  is the velocity of mixture particles  $i$  and  $j$ , respectively;  $m_{ij}$  and  $\rho_{ij}$  are the total mass and total density of the particle  $j$ .

The pore water pressure head is updated using Eq.(32) (Lian et al., 2023):

$$h_i^{t+1} = \frac{\sum_{j=1}^N V_j k_{ij}^{mn} \mathcal{S}^{mn} \tilde{F}_{ij} h_j^t + B_{ij} + \frac{C_{sr} h_i^t}{\Delta t_w}}{\left( \sum_{j=1}^N V_j k_{ij}^{mn} \mathcal{S}^{mn} \tilde{F}_{ij} + \frac{C_{sr}}{\Delta t_w} \right)} \quad (32)$$

where  $k_{ij}^{mn} = (k_i^{mn} + k_j^{mn})/2$  is the average permeability coefficient between particle  $i$  and  $j$ ;  $\Delta t_w$  is the critical time step of seepage flow;  $C_{sr} = \phi dS_r/dh$  is the specific storage term obtained from the SWCC and  $B_{ij}$  is the pore water pressure source term.  $B_{ij}$  is defined as:

$$B_{ij} = -S_r \nabla \cdot \mathbf{v}_s + \frac{k_{ij}}{g} \nabla \cdot \left( \frac{d\mathbf{v}_s}{dt} \right) + \nabla \cdot [k_{ij} (\nabla z)] - E_i \quad (33)$$

with  $E_i$  being the error source term, which is computed only within the porous media (excluding surface particles):

$$E_i = k_{ij}^{mn} \frac{\partial h_i}{\partial x_{ji}^m} \sum_{j=1}^N V_j x_{ji}^n \mathcal{S}^{mn} \tilde{F}_{ij} \quad (34)$$

The momentum balance is approximated as follows:

$$\left( \frac{d\mathbf{v}_s}{dt} \right)_i = \sum_{j=1}^N m_{ij} \left( \frac{(\sigma'_i - S_{ei} p_{wi} \mathbf{m})}{\rho_{ti}^2} + \frac{(\sigma'_j - S_{ej} p_{wj} \mathbf{m})}{\rho_{ij}^2} + \mathbf{C}_{ij} \right) \nabla_i W_{ij} + \mathbf{b}_i + \mathbf{F}_{di} \quad (35)$$

where  $m_{ij}$  is the total mass of the soil mixture particle  $j$ ;  $\rho_{ti}$  and  $\rho_{ij}$  are the total density of the soil mixture particles  $i$  and  $j$ ;  $\sigma'_i$  and  $\sigma'_j$  are the effective stress of particles  $i$  and  $j$ ;  $p_{wi}$  and  $p_{wj}$  are the pore water pressure of particles  $i$  and  $j$ ;  $S_{ei}$  and  $S_{ej}$  is the effective degree of saturation of particles  $i$  and  $j$ ;  $\mathbf{C}_{ij}$  is the artificial viscosity used to remove stress fluctuations (Bui et al., 2008);  $\mathbf{b}_i$  is gravity force vector of particle  $i$ ;  $\mathbf{F}_{di} = -\mu_d \mathbf{v}_{si}$  is damping force used at initial state to get stable stress distribution (Bui and Fukagawa, 2013);  $\mu_d$  is damping coefficient.

#### 3.3. SPH time integration

The positions of SPH mixture particles are updated as follows:

$$\mathbf{r}_s^{t+1} = \mathbf{r}_s^t + \frac{\mathbf{v}_s^t + \mathbf{v}_s^{t+1}}{2} \Delta t_s \quad (36)$$

where  $\mathbf{r}_s^t$  and  $\mathbf{r}_s^{t+1}$  are the positions of the SPH particle at time  $t$  and  $t + 1$ , respectively.

The critical time step  $\Delta t_s$  for soil motion is determined by the following equation:

$$\Delta t_s \leq C_{CFL} \frac{l}{c_s} \quad (37)$$

where  $C_{CFL}$  is the Courant number, normally taken as 0.2;  $l$  is the length scale of the initial numerical discretisation;  $c_s$  is the sound speed of soil.

The critical time step of the seepage flow  $\Delta t_w$  is defined as follows:

**Table 1**

Parameters of constitutive model and hydraulic model.

Parameters	Value	Parameters	Value
The slope of the swelling line $\kappa$	0.01	The slope of the NCL $\lambda_0$	0.121
Reference critical void ratio $e_{ref}$	2.78	Poisson's ratio $\mu$	0.3
Critical state stress ratio $M$	1.1	Reference stress $p_c$ (Pa)	1
Constant parameter $a_1$ for $\lambda(S_e)$	1.85	Parameter $\alpha$	0.077 (1/m)
Parameter $\phi$	3	Parameter $g_n$	1.5
Parameter $g_c$	-0.3		

$$\Delta t_w \leq \frac{\phi \gamma_w h_{sm}^2}{K_w k_{sat}} \quad (38)$$

where  $\phi$  is the porosity;  $\gamma_w$  is the specific weight of water;  $K_w$  is the water bulk modulus;  $k_{sat}$  is the saturated permeability coefficient;  $h_{sm}$  is the smoothing length of the kernel function. It is noted that in fully coupled hydro-mechanical simulations, an adaptive time-stepping algorithm (Lian et al., 2022, Ma et al., 2024) is used to optimise computational efficiency.

#### 4. Validation and verification of the unsaturated constitutive model

This section presents the validation and verification of the adopted simplified unsaturated constitutive model through element level tests against experimental data on unsaturated soils, SPH simulations of granular collapse under large deformation compared with experimental results, and simple shear tests using SPH to verify implementation and assess model performance under varying void ratios and suction levels.

##### 4.1. Element level test

In this section, the performance of the unsaturated model is evaluated in element level against experimental data reported by Sun et al., (2007). In Sun et al. (2007) study, they investigated the mechanical

response of unsaturated Pearl clay through triaxial compression and wetting tests on samples compacted to different initial void ratios. The experimental procedure involved three loading stages. In the first stage, Pearl clay samples with varying initial void ratios were subjected to triaxial compression under constant suction conditions until the ratio of the first net principal stress to the third net principal stress reached 1.5. In the second stage, the specimens were soaked to eliminate suction while maintaining the constant net stress ratio. In the final stage, triaxial compression was applied under zero suction conditions until failure. In this study, two experimental cases from Sun et al., (2007) were selected for numerical simulation: one with an initial void ratio of 1.41 and the other with an initial void ratio of 1.27. In both cases, a constant suction of 147 kPa was applied during the first triaxial compression stage. The material parameters adopted for the constitutive and hydraulic models are summarised in Table 1.

Fig. 3 presents a comparison between the experimental results, the numerical predictions from the current model, and those from original model by Zhou and Sheng (2015). In the figure, the dotted lines represent experimental data, solid lines correspond to the current model, and dashed lines show the results from Zhou and Sheng (2015). Red curves indicate results obtained under a smaller initial void ratio ( $e_0 = 1.27$ ), while blue curves correspond to a larger initial void ratio ( $e_0 = 1.41$ ). Although the current model employs a simplified hydraulic model compared to Zhou and Sheng, (2015), it still successfully demonstrates that a smaller initial void ratio ( $e_0 = 1.27$ ) significantly reduces soaking-induced deviatoric and volumetric strain compared to a larger void ratio ( $e_0 = 1.41$ ). Furthermore, as the soil becomes denser, dilative volumetric strains gradually develop, accompanied by an increase in deviatoric stress. The variations in the degree of saturation are also captured. These findings highlight the ability of the adopted unsaturated constitutive model to effectively reproduce the influence of void ratio on the hydro-mechanical behaviour of unsaturated soils.

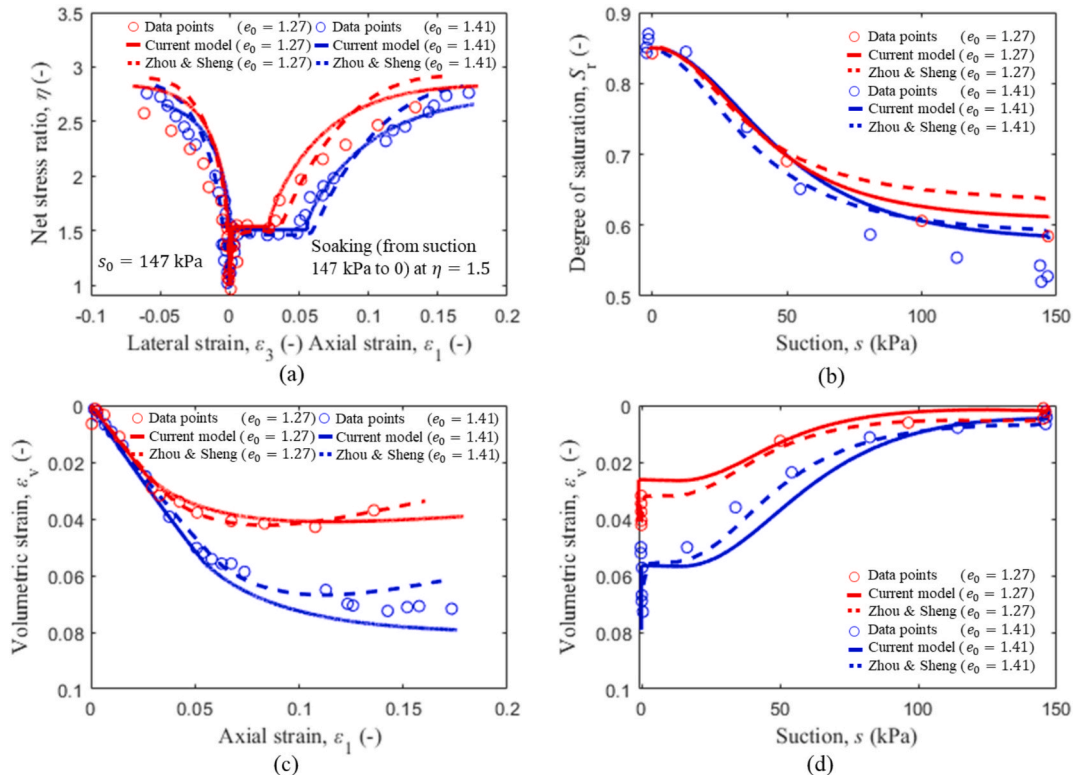


**Fig. 3.** Evaluation of the current model against the Zhou and Sheng (2015) model and experimental data.

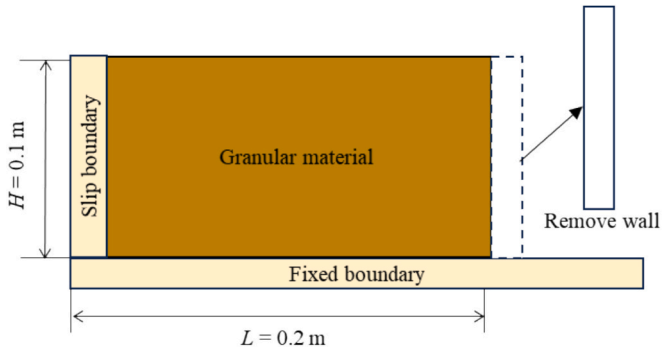


Fig. 4. SPH set up for granular collapse.

Table 2

Parameters of the constitutive model in the granular collapse test.

Parameters	Value	Parameters	Value
The slope of the swelling line $\kappa$	0.008	The slope of the NCL $\lambda_0$	0.05
Reference critical void ratio $e_{ref}$	1.3	Poisson's ratio $\mu$	0.3
Critical state stress ratio $M$	0.57	Reference stress $p_c$ (Pa)	1
Constant parameter $a_1$ for $\lambda(S_e)$	2		

#### 4.2. Granular collapse test

This section evaluates the capability of the constitutive model to capture the effects of void ratio under large deformations within the SPH numerical framework, in comparison with experimental data from granular material collapse tests. Given the limited availability of experimental data on unsaturated granular collapse, a special experimental case (Bui et al., 2008) involving zero suction force is adopted for

constitutive model validation. The geometry is depicted in Fig. 4, with dimensions of 0.2 m in length and 0.1 m in height, as referenced from Bui et al., (2008). Aluminium bars with various diameters (1 mm and 1.5 mm) were used as the granular material in the experiment. In the setup of SPH simulation, the left and right retaining walls are assumed to have free-slip boundaries, while the bottom boundary used non-slip boundary condition. These boundary conditions follow same setup with Bui et al. (2008). Considering both computational efficiency and accuracy, the initial SPH particle spacing is set to 0.0025 m with a total of 3920 SPH particles used. The initial stress distribution results from gravity loading. At the start of the simulation, the right wall is removed to trigger the granular collapse. The constitutive model parameters adopted in this test are listed in Table 2 and are selected to provide the best fit to the experimental observations.

Fig. 5 shows the numerical results of the granular collapse with zero suction. The surface configuration and failure curve observed in the experiment are well captured with the initial void ratio ( $e_0$ ) in the range of 0.95 to 1.05, which represents a loose state. The SPH studies by Wang et al. (2024) and Zhu et al. (2024) employed advanced critical state soil models and reported results consistent with similar void ratio values. Additionally, similar final failure patterns have been reproduced using the material point method (Sołowski and Sloan, 2015) and the smoothed particle finite element method (Zhang et al., 2021, Yuan et al., 2019). However, these latter studies used an elastic-perfectly plastic material with the Mohr–Coulomb yield criterion and did not report void ratio values, so no direct comparison was made. This demonstrates that the adopted constitutive model implemented in SPH can correctly model the large deformation problems with variable void ratios.

#### 4.3. Simple shear test

This section focuses on verifying the correct implementation of the

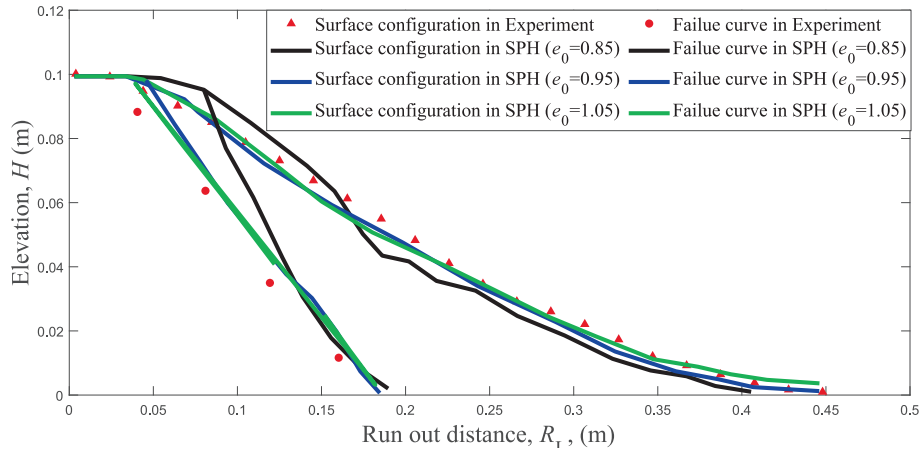


Fig. 5. Comparison of geometric configurations for granular collapse.

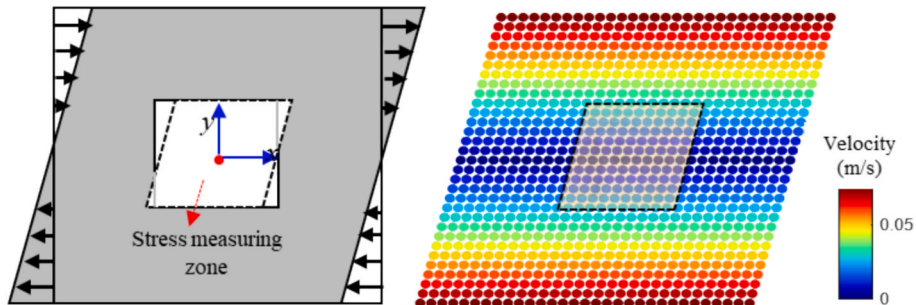


Fig. 6. Simple shear test in SPH.

**Table 3**

Parameters of constitutive model in simple shear test.

Parameters	Value	Parameters	Value
The slope of the swelling line $\kappa$	0.005	The slope of the NCL $\lambda_0$	0.175
Reference critical void ratio $e_{ref}$	2.65	Poisson's ratio $\mu$	0.3
Critical state stress ratio $M$	1	Reference stress $p_c$ (Pa)	1
Constant parameter $a_1$ for $\lambda(S_e)$	1.65		

constitutive model and its ability to predict the effects of initial void ratio and suction within the SPH framework. A simple shear test is simulated following the studies of [Bui and Nguyen, \(2021\)](#), [Nguyen et al., \(2025\)](#) and [Nonoyama et al., \(2015\)](#). In this study, simple shear tests are conducted under undrained conditions, with constant suction and constant volume. It is important to note that in experiment the constant suction is maintained by simultaneously increasing both the air pressure and the water pressure by the same amount ([Wheeler and Sivakumar, 1995](#)). As illustrated in [Fig. 6](#), the simple shear test setup consists of a central representative soil element surrounded by boundary regions. Both the soil and boundary are represented by SPH particles with identical material properties. While particles in the central region move freely, those in the boundary region are assigned a controlled velocity field. In this case, the initial SPH particle spacing is set to 0.005 m. The entire rectangular domain measures 0.15 m  $\times$  0.15 m, while the internal soil domain occupies a 0.05 m  $\times$  0.05 m area. The solid particle density is 2650 kg/m<sup>3</sup>, and an initial confining stress  $p'$  of 20 kPa is applied. The parameters for the unsaturated model are listed in [Table 3](#). These parameters are typical of silty soil properties and can be referenced from the constitutive model studies of [Zhou and Sheng \(2015\)](#) and [Yu \(1998\)](#). The hydraulic parameters are the same as those used in [Fig. 1](#). The SPH simple shear test results are compared with those from a

single-element test conducted in MATLAB.

[Fig. 7](#) (a) and (b) illustrates the performance of the constitutive model under different density states by varying the void ratios under zero suction (i.e.  $s = 0$  kPa). [Fig. 7](#) (a) demonstrates typical dense sand behaviour with strain hardening for an initial void ratio of  $e_0 = 0.67$ , and medium-dense sand behaviour for  $e_0 = 0.82$ , whereas loose sand behaviour is observed for  $e_0 = 1$ . [Fig. 7](#) (b) shows the relationship between  $p'$  and  $q$ , where the final deviatoric stress reaches the critical state, closely aligning with the critical state line (CSL). These results indicate that the constitutive model effectively captures the mechanical behaviour of both dense and loose sands by varying the initial void ratio.

[Fig. 7](#) (c) and (d) presents the constitutive performance under varying initial suction levels at same initial void ratio (i.e.  $e_0 = 0.82$ ). As observed, increasing the initial suction from 0 kPa to 25 kPa leads to a significant enhancement in both the deviatoric peak and residual stresses of the soil. The final deviatoric stresses for all cases converge closely along the same critical state line. Apart from the direct contribution of suction to the enhancement of soil effective stress, the higher suction levels contribute to enhanced soil yield strength through the expansion of the yield surface.

## 5. Rainfall-induced failure analysis of homogeneous and heterogeneous slopes

### 5.1. Numerical setup

This section presents the SPH numerical setup for a synthetic sandy soil embankment, based on the study by [Liu and Wang \(2021\)](#). The geometry is illustrated in [Fig. 8](#), with the slope having a height of 14 m and a bottom length of 40 m. The slope angle is set at 35.5 degrees. The left, right, and bottom boundaries are defined by impermeable walls.

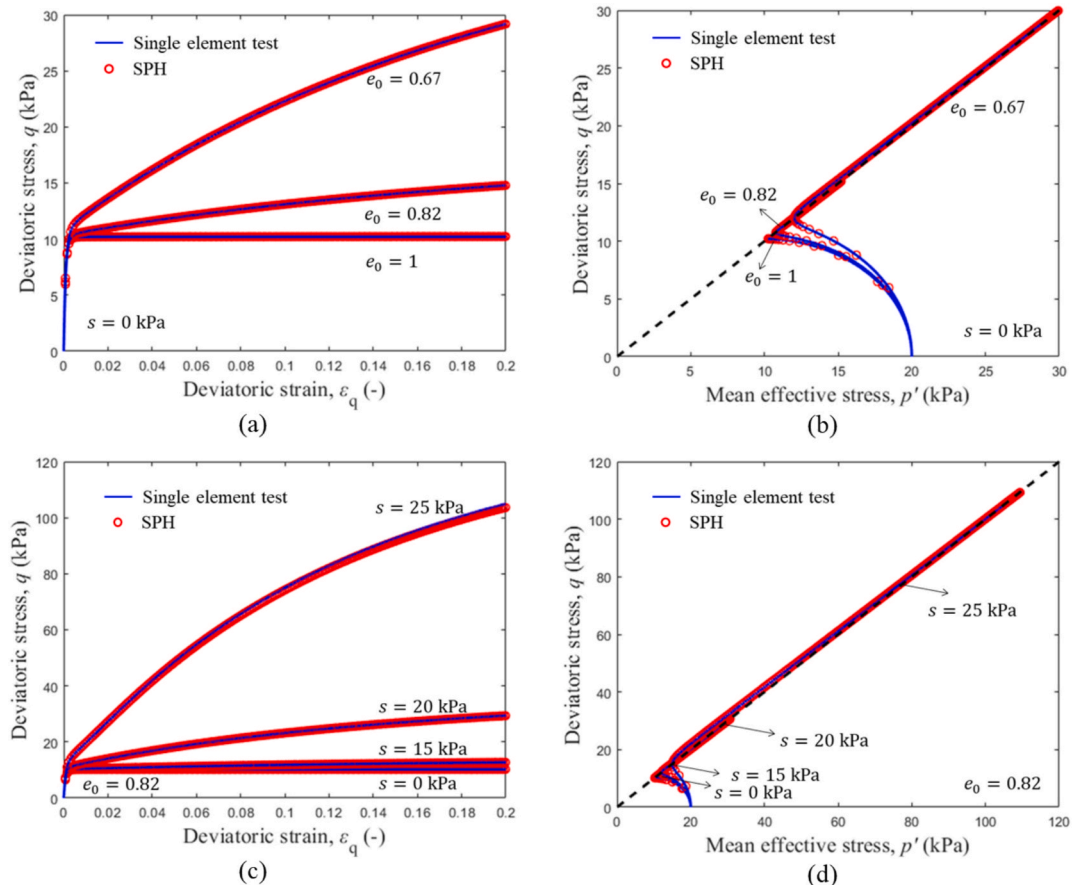


**Fig. 7.** Influence of initial void ratio and initial suction on the constitutive model performance.



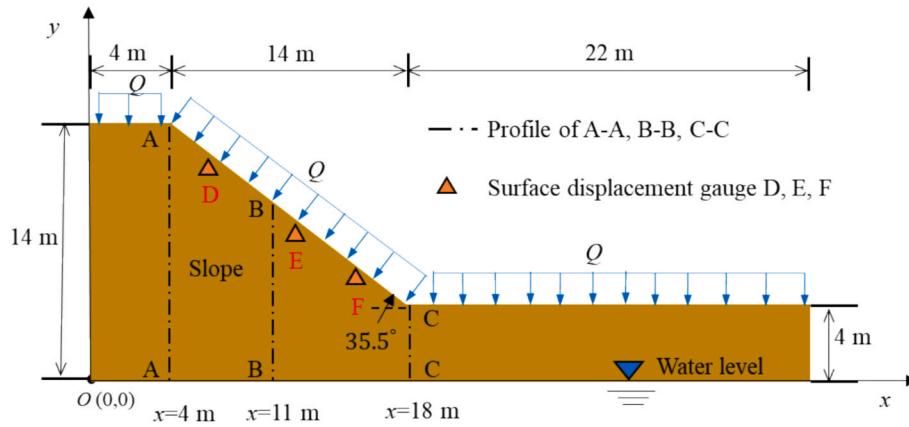
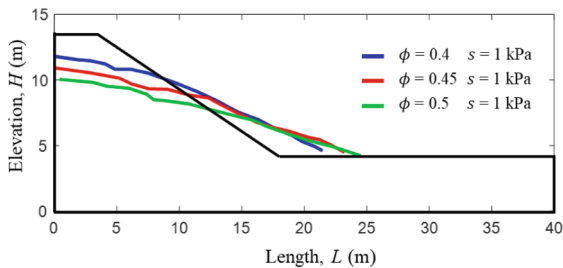


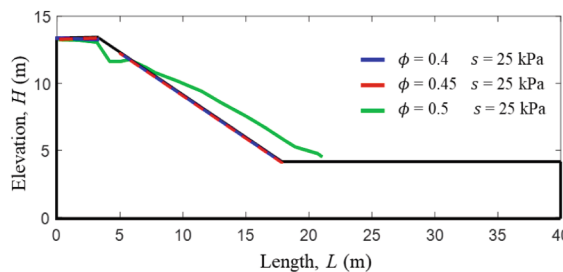
Fig. 8. Geometry of the synthetic embankment and boundary conditions.

**Table 4**  
Selected mean value of porosity and suction in slope stability test.

Cases	Mean porosity ( $\phi$ )	Suction (s)	Stability	Run-out distance	Sliding area
1	0.4	1 kPa	No	3.4 m	35.5 m <sup>2</sup>
2	0.45	1 kPa	No	5.2 m	41.1 m <sup>2</sup>
3	0.5	1 kPa	No	6.5 m	46.8 m <sup>2</sup>
4	0.4	25 kPa	Yes	0.0 m	0.0 m <sup>2</sup>
5	0.45	25 kPa	Yes	0.0 m	0.0 m <sup>2</sup>
6	0.5	25 kPa	No	2.9 m	33.7 m <sup>2</sup>



(a) Suction = 1 kPa



(b) Suction = 25 kPa

Fig. 9. Surface profile of the slope failure.

The left and right boundaries are modelled as free-slip boundaries, while the bottom boundary is non-slip, consistent with the setup used in the granular flow test. If the rainfall boundary condition is activated, the surface boundary is subjected to a constant water flux. The soil grain density is 2650 kg/m<sup>3</sup> and the water density is 1000 kg/m<sup>3</sup>. An initial saturated permeability coefficient is assumed as  $1 \times 10^{-4}$  m/s. The soil water characteristic curve (SWCC) parameters are assumed as follows:  $S_{\text{sat}} = 1$ ,  $S_{\text{res}} = 0$ ,  $g_n = 2.286$ ,  $g_c = -0.563$ ,  $g_l = 0$ ,  $\alpha = 0.5$  (1/m), and  $\varphi = 0.2$ , consistent with the parameters used in Fig. 1. The parameters for the constitutive model are the same as those shown in Table 3.

Considering both computational efficiency and accuracy, a total of 28,585 particles with a spacing of 0.1 m was used in this case. Thanks to SPH's non-local interpolation feature (Vignjevic et al., 2014), the slope failure simulation employed the same smoothing length as the granular collapse case, ensuring comparable numerical resolution and accuracy despite the difference in physical dimensions. To compare the failure behaviour of homogeneous and heterogeneous slopes, numerical data along profiles A-A ( $x = 4$  m), B-B ( $x = 11$  m), and C-C ( $x = 18$  m) are presented in the discussion section. Additionally, surface displacement data from gauges D, E, and F located at ( $x = 8$  m,  $y = 10.5$  m), ( $x = 12$  m,  $y = 7.8$  m), and ( $x = 16$  m,  $y = 4.8$  m) are included for displacement analysis.

## 5.2. Initial stability test of homogeneous slope

An initially stable slope is essential for modelling rainfall-induced slope failure. The initial stability of the slope is significantly influenced by both void ratio and suction. This section investigates the effect of typical mean values of porosity (or void ratio) and suction on the initial stability of the slope without rainfall, based on the adopted constitutive model parameters. The time step for the fully coupled simulation is set as  $\Delta t_s = \Delta t_w = 5 \times 10^{-6}$  s. Table 4 presents the selected mean values of porosity and suction used in the tested cases. Slope stability is defined by a runout distance threshold of zero meters. Porosities of 0.4, 0.45, and 0.5 were tested under uniformly distributed suction conditions of 1 kPa and 25 kPa. It is observed that under low suction (1 kPa), slopes with porosities ranging from 0.4 to 0.5 are unstable, with both runout distance and sliding area increasing as the initial porosity increases. At a suction level of 25 kPa, slopes with porosities of 0.4 and 0.45 become stable, indicating that higher suction levels significantly enhance initial slope stability. However, the slope with a porosity of 0.5 remains unstable, although both runout distance and sliding area are reduced. In this case, an even higher suction level is required to achieve overall stability for looser soils.

Fig. 9 (a) and (b) illustrate the surface profiles of slope failures under different conditions. Fig. 9 (a) shows that as porosity increases, the soil material becomes looser and more susceptible to failure, leading to deeper slope failures and longer run-out distances. Consequently, the sliding area increases significantly. Fig. 9 (b) shows that higher suction enhances soil strength, thereby reducing both the run-out distance and sliding area compared to the lower suction condition at the same void ratio. Based on these observations, a mean porosity of 0.4 with a suction of 25 kPa is selected as the base case to investigate rainfall-induced slope failure in the following section.

## 5.3. Homogeneous slope under heavy rainfall

In this section, a uniform porosity of 0.4 and a uniform suction of 25

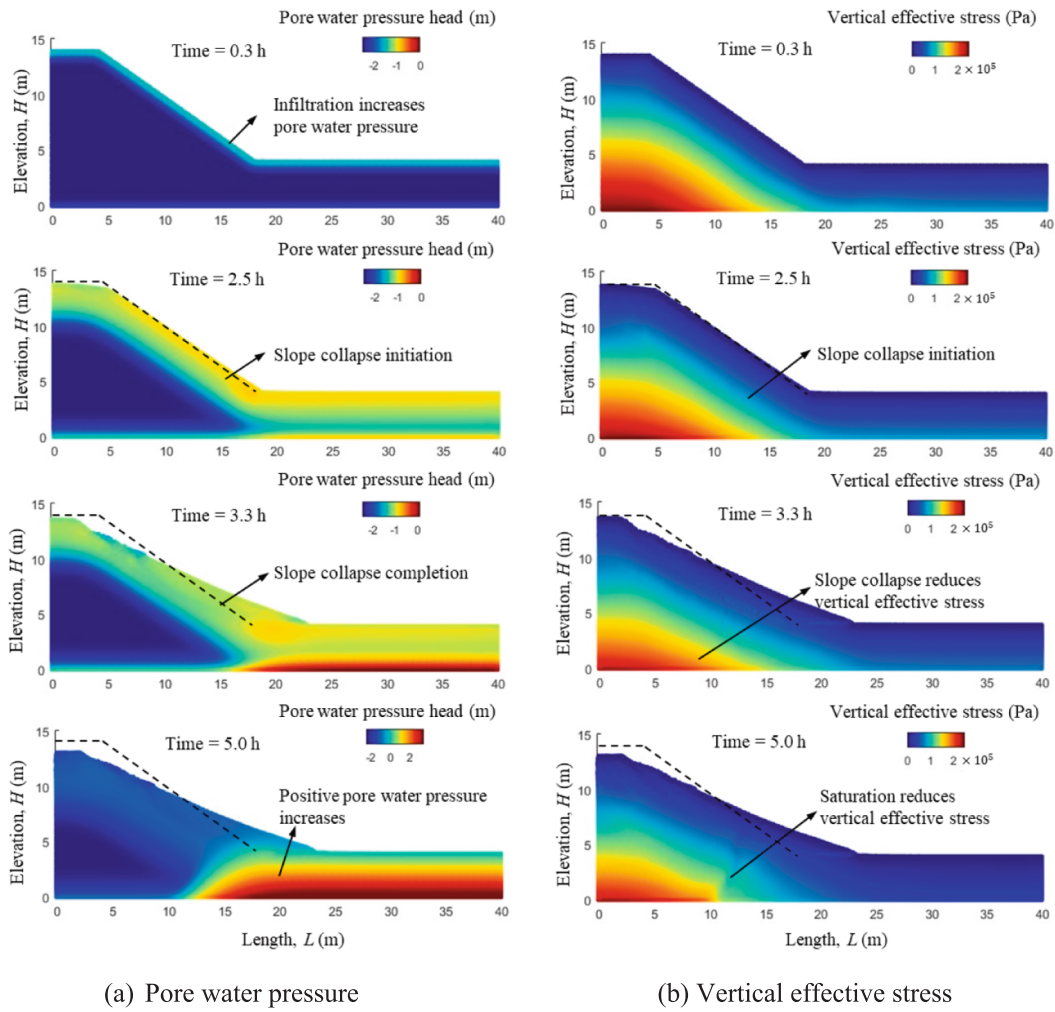


Fig. 10. Evolution of pore water pressure and vertical effective stress for a homogeneous slope.

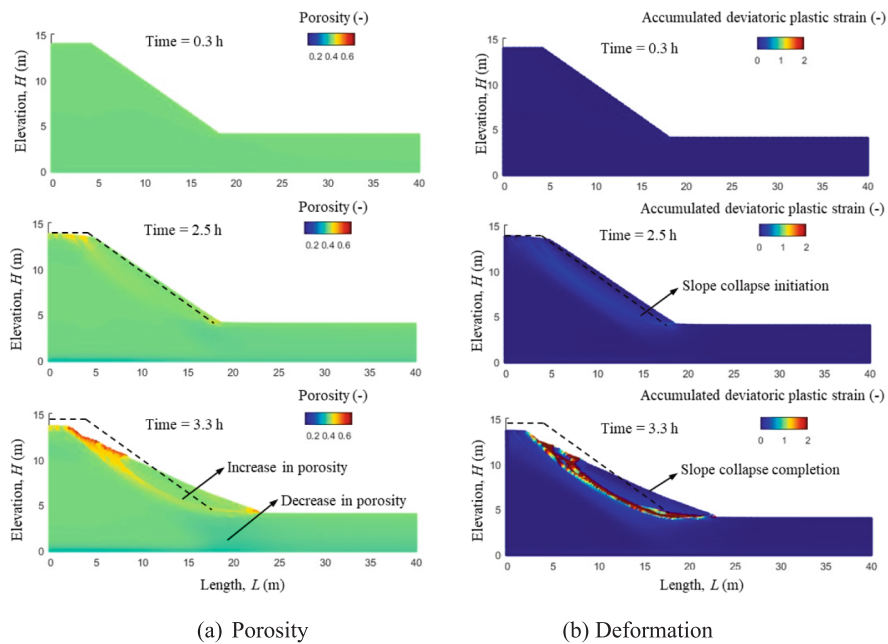


Fig. 11. Evolution of porosity and deformation for a homogeneous slope.

**Table 5**  
Statistics of porosity.

Parameter	Distribution	Mean value	COV	Correlation length $\theta(\phi)$
Porosity $\phi$	Log-normal	0.4	0.15	3

kPa are applied to the slope. Heavy rainfall is simulated by applying a surface flux of  $Q = 5 \times 10^{-5}$  m/s to the slope surface boundaries. To model infiltration runoff, a drainage condition (i.e., no ponding water on the slope surface) is simulated by setting any positive pore water pressure on the slope surface to zero. An adaptive time-stepping scheme (Lian et al., 2022, Ma et al., 2024) is employed to accelerate the infiltration process, with the initial time steps set as  $\Delta t_s = 5 \times 10^{-6}$  s and  $\Delta t_w = 5 \times 10^{-2}$  s. Fig. 10 presents the numerical results of a homogeneous slope failure. Fig. 10 (a) illustrates the evolution of pore water pressure. Initially, the soil sample exhibits a uniform suction of 25 kPa. As infiltration progresses, the pore water pressure gradually propagates from the surface into the soil body. By 2.5 h, water infiltration causes the negative pore water pressure (suction) to reduce significantly in the slope. The loss of suction leads to a significant reduction in the soil's yield strength, which abruptly triggers slope collapse, known as wetting-induced slope failure. The final run-out distance is approximately 4.9 m. The slope collapse is completed at around 3.3 h. And with further water infiltration, positive pore water pressure builds up at the bottom of the foundation at 5 h. Fig. 10 (b) shows the evolution of vertical effective stress. On the one hand, slope collapse leads to a reduction in effective

stress. On the other hand, during the saturation process, decreasing suction and the gradual increase in positive pore water pressure further contribute to the reduction in effective stress.

Fig. 11 (a) shows the evolution of porosity. Initially, a uniform porosity of 0.4 is applied throughout the soil body. As deformation occurs, porosity significantly increases within the shear band due to the shear-induced dilation. The soil becomes looser in the deformed zone. The soil's porosity slightly decreases in the foundation zone due to the overburden pressure from the soil above. The deformation is characterised by the accumulated plastic strain, which exhibits a similar spatial and temporal evolution to porosity, as shown in Fig. 11 (b). As can be seen, an evident shear band forms with the progression of the slope failure.

#### 5.4. Heterogeneous slope with spatial variability of void ratio under heavy rainfall

The heterogeneous porosity distribution of the slope is generated using the local average subdivision (LAS) (Fenton and Vanmarcke, 1990, Fenton and Griffiths, 2007) random field generation method. The LAS method generates spatially correlated random fields through a hierarchical averaging process. The method begins by dividing the domain into a set of uniformly sized blocks. Each block is then recursively subdivided into smaller blocks to progressively refine the spatial resolution. At each level of subdivision, random values are assigned in a manner that preserves the desired statistical properties, such as variance and spatial correlation. This method has been widely applied in

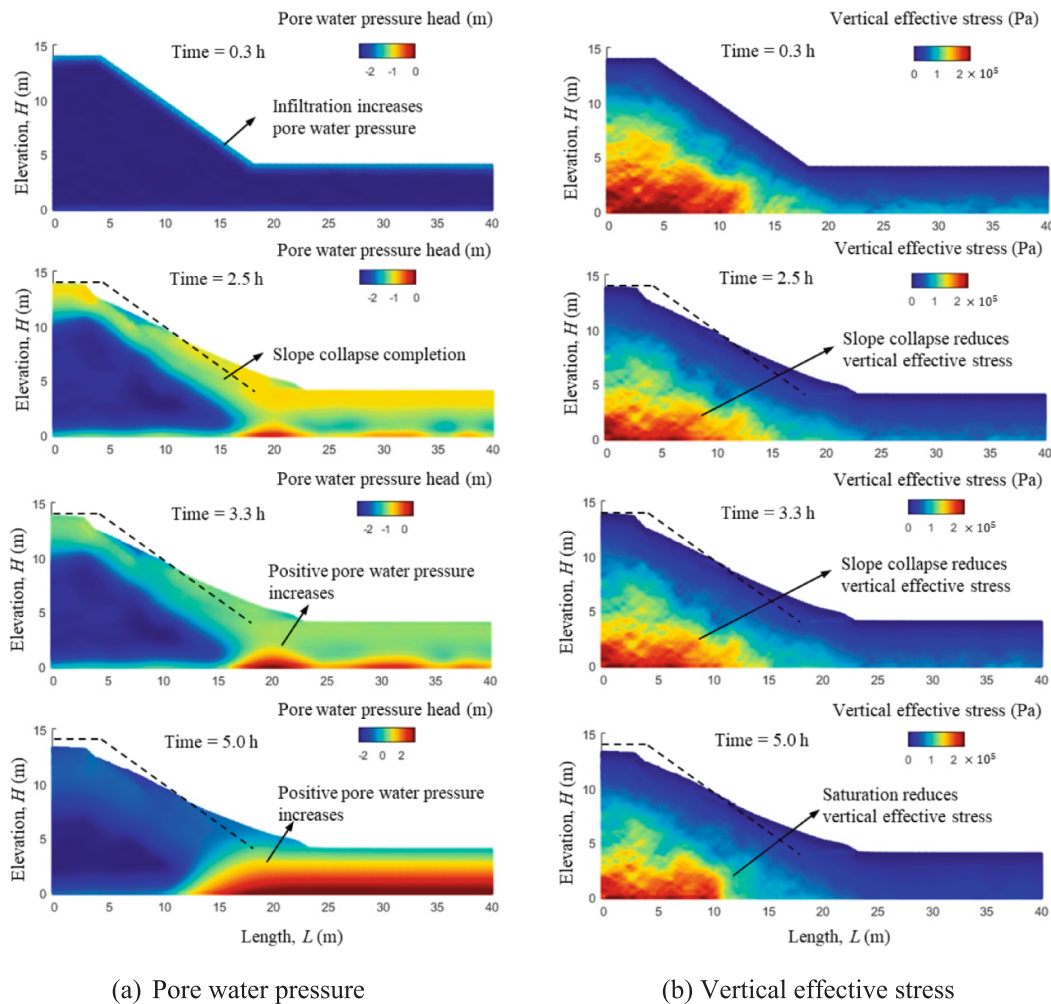


**Fig. 12.** Evolution of pore water pressure and vertical effective stress for a heterogeneous slope.

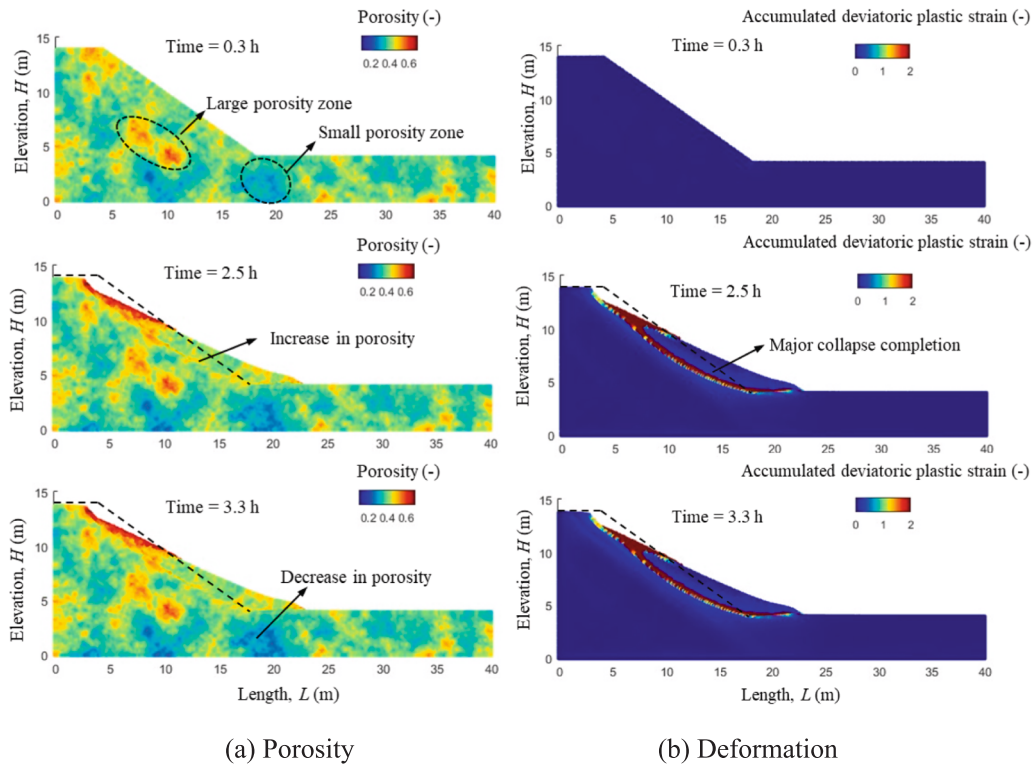


Fig. 13. Evolution of porosity and deformation for a heterogeneous slope.

geotechnical engineering and is adopted in this study.

Although Gaussian random field is commonly used to model spatial variability because of its mathematical convenience. It is not appropriate when the random variable must be strictly positive, such as porosity. To overcome this, we use a Gaussian random field that is transformed into a lognormal random field at the particle level. This method has been widely adopted by researchers such as Le et al. (2019), Dyson and Tolooiyan (2019), Cho (2010), and Griffiths et al. (2009) to model the spatial distribution of soil properties including friction angle, cohesion, and porosity. The statistic of porosity of this tested case is shown in Table 5. In Table 5, the mean porosity  $\mu(\phi)$  is 0.4. Following Le et al. (2015) and Fang et al. (2024), the coefficient of variation (COV) typically ranges from 0.05 to 0.3, as larger values can produce porosity outside the physically reasonable range (0–1). In this study, a COV of 0.15 was selected, resulting in heterogeneous porosity values between 0.15 and 0.65, which lie within the range reported in previous studies (e.g., Le et al., 2012, Le et al., 2013). The horizontal correlation length  $\theta(\phi)$  is assumed to be equal to the vertical correlation length. An appropriate value must be selected to ensure the soil's initial stability while adequately representing void ratio variability. Uzielli et al. (2007) suggested a vertical correlation length of approximately 3 m for organic silty clay, while Le et al. (2015) adopted 2 m when studying the stability of rainfall-induced slopes. Based on these references, a value of 3 m is considered practically reasonable for the current study. All other variables and constitutive model parameters remain consistent with those used in the homogeneous soil simulations.

Fig. 12 (a) illustrates the evolution of pore water pressure in the heterogeneous soil. The random distribution of porosity dominates the variation in the degree of saturation and permeability coefficient, as both are directly linked through Eq. (5) and Eq. (8). And smaller porosity accelerates the evolution of the pore water pressure in unsaturated soil, as shown in Eq. (3). Initially, uniform suction of 25 kPa is applied to a heterogeneous slope. At  $t = 2.5$  h, the pore water pressure increases more rapidly than in the previous homogeneous slope and exhibits a heterogeneous distribution. At this point, the slope collapse is almost

complete, and the initiation of failure occurs approximately 30 min earlier compared to the previous scenario. The final runout distance is greater, measuring approximately 5.1 m. Following the saturation of the slope, the pore water pressure becomes positive and continues to rise after 3.3 h. At  $t = 5$  h, in the fully saturated zone, the pore water pressure distribution returns to a homogeneous state, indicating that the influence of the heterogeneous porosity distribution has disappeared. Fig. 12 (b) shows a significant uneven distribution of effective stress, primarily attributed to variations in the density state. At  $t = 2.5$  h, slope collapse causes the drop in the effective stress. After  $t = 3.3$  h, the saturation process and the buildup of positive pore water pressure cause a further reduction in effective stress.

Fig. 13 presents a representative distribution of heterogeneous porosity. Typical large and small porosity zones are shown in Fig. 13 (a). The existence of initial large and small porosity zones significantly affects the temporal and spatial evolution of the degree of saturation and the permeability coefficient, which will be discussed in the following paragraphs. Similar to the results observed in homogeneous slope collapse, the porosity within the shear band increases, while the soil's porosity in the foundation zone, beneath the accumulated collapsed soil, slightly decreases. Fig. 13 (b) illustrates the large deformation process of the slope. The notable differences compared to the homogeneous slope are the earlier onset of failure and the slightly longer run-out distance.

Fig. 14 presents the temporal and spatial variability of the degree of saturation and permeability coefficient. Fig. 14 (a) shows that the distribution of the degree of saturation follows an opposite pattern to that of porosity. In zones with low porosity, a high initial degree of saturation is observed in the unsaturated zone, whereas in zones with high porosity, a low initial degree of saturation is present in the unsaturated zone. When slope collapse occurs, the large deformation increases porosity, which may cause desaturation, reducing the degree of saturation. This phenomenon is particularly evident in surface zones experiencing large deformation. After full saturation, the non-homogeneous distribution of the degree of saturation vanishes, reducing its effects on soil's hydraulic properties. Fig. 14 (b) demonstrates the influences of



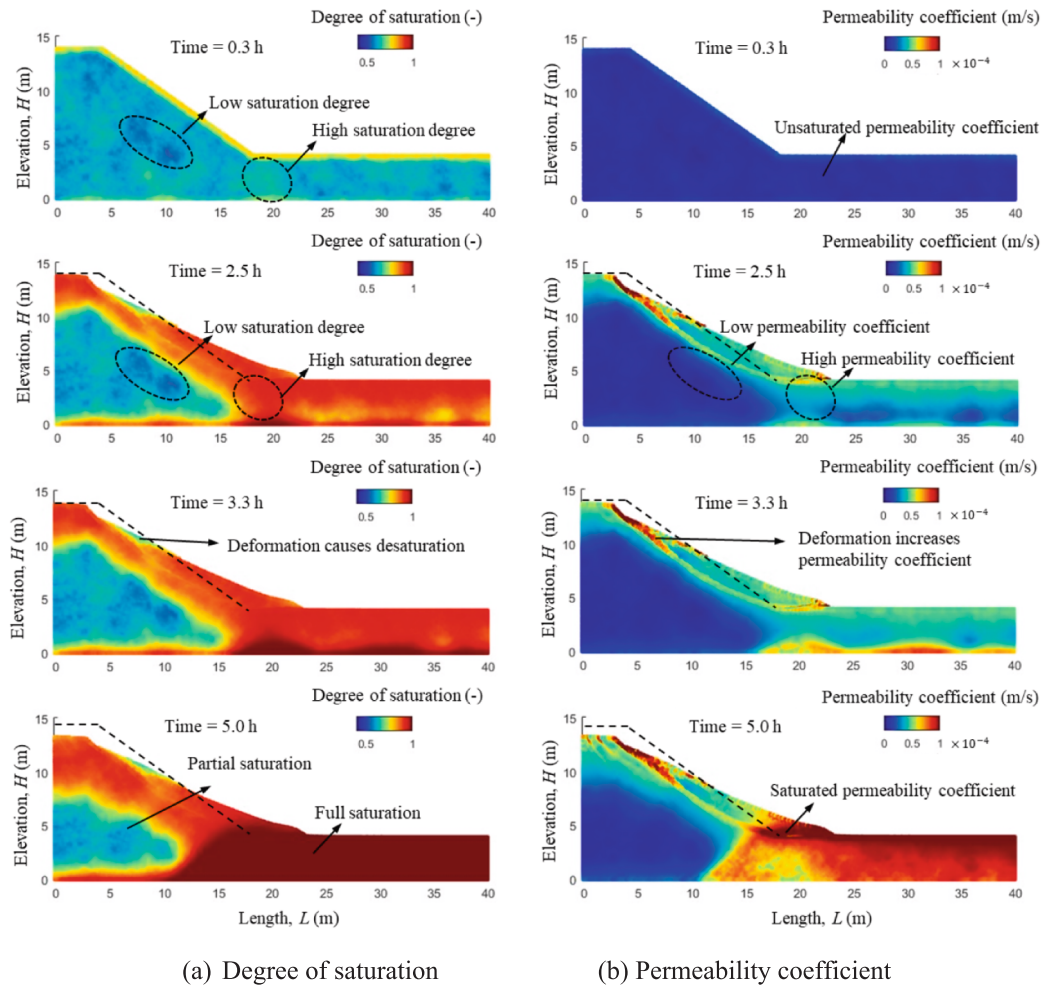


Fig. 14. Evolution of permeability and degree of saturation for a heterogeneous slope.

porosity on the permeability coefficient. At  $t = 0.3$  h, under unsaturated conditions, the permeability coefficient is at least an order of magnitude (10 times) lower than the saturated coefficient. As a result, this correspondence between porosity and permeability coefficient is not evident. At  $t = 2.5$  h, it can be observed that, in the unsaturated zone, smaller porosity is generally associated with an increased relative unsaturated permeability coefficient. This explains that local zones of low porosity contribute to faster infiltration in heterogeneous soils under unsaturated conditions. These findings are consistent with the results presented in Fig. 1 (b). In Fig. 14 (b), after  $t = 2.5$  h, porosity increases significantly in the deformed zone, leading to desaturation. As a result of this increase in porosity, the total permeability coefficient also rises. That is because the total permeability coefficient is governed by the coupling effects of degree of saturation and porosity, as demonstrated in Eq. (4). At  $t = 5$  h, at the saturated foundation zone, large porosity contributes to higher saturated permeability coefficients.

### 5.5. Discussion

To further demonstrate the influence of porosity's spatial variability on slope failure, Fig. 15 to Fig. 17 present comparisons of porosity, pore water pressure, and mean effective stress profiles between the homogeneous case and the heterogeneous case ( $COV = 0.15$ ) along profiles A-A, B-B, and C-C of the slope. Fig. 15 presents the comparison of porosity evolution. The profiles are plotted starting from 0.5 m depth, within the interior of the slope. In the homogeneous case, porosity along profiles A-A and B-B remains nearly constant at 0.4 throughout the slope over time.

The porosity along profile C-C initially is 0.4 and shows a slight decrease, as previously demonstrated, due to the accumulation of collapsed soil over this profile. In contrast, for the heterogeneous case with  $COV = 0.15$ , profiles A-A, B-B, and C-C show variations in porosity with elevation due to random spatial distributions. The porosity along profile A-A is higher than the average value of 0.4 between 8 m to 10 m, and lower than 0.4 at elevations below 8 m. Along profile B-B, the porosity exceeds the average value above 3 m. For profile C-C, the porosity remains below the average value throughout the entire profile and also exhibits a decreasing trend over time.

Fig. 16 shows the evolution of pore water pressure along profiles A-A, B-B, C-C. For the homogeneous slope at profile A-A, the initial pore water pressure head is uniform at  $-2.5$  m. As infiltration progresses, the top of the slope becomes saturated by  $t = 2.5$  h. Additionally, because the bottom boundary is under undrained conditions, the pore water pressure head increases rapidly at the base due to water accumulation. In contrast, after  $t = 2.5$  h, water infiltrates more slowly between 8 m and 10 m along the profile compared to homogeneous soil, due to the larger porosity in this zone. It should be emphasized that the evolution of pore water pressure within the current profile is affected not only by its intrinsic properties but also by the porosity distribution of adjacent profiles. This reflects the impacts of preferential flow paths driven by spatial porosity variability, as illustrated in Fig. 13 (a).

Similarly, along profile B-B at elevations above 3 m, the pore water pressure in the heterogeneous slope increases slowly compared to the homogeneous case, due to the abrupt increase in porosity within this section of the profile. In profiles C-C, slightly faster water infiltration is

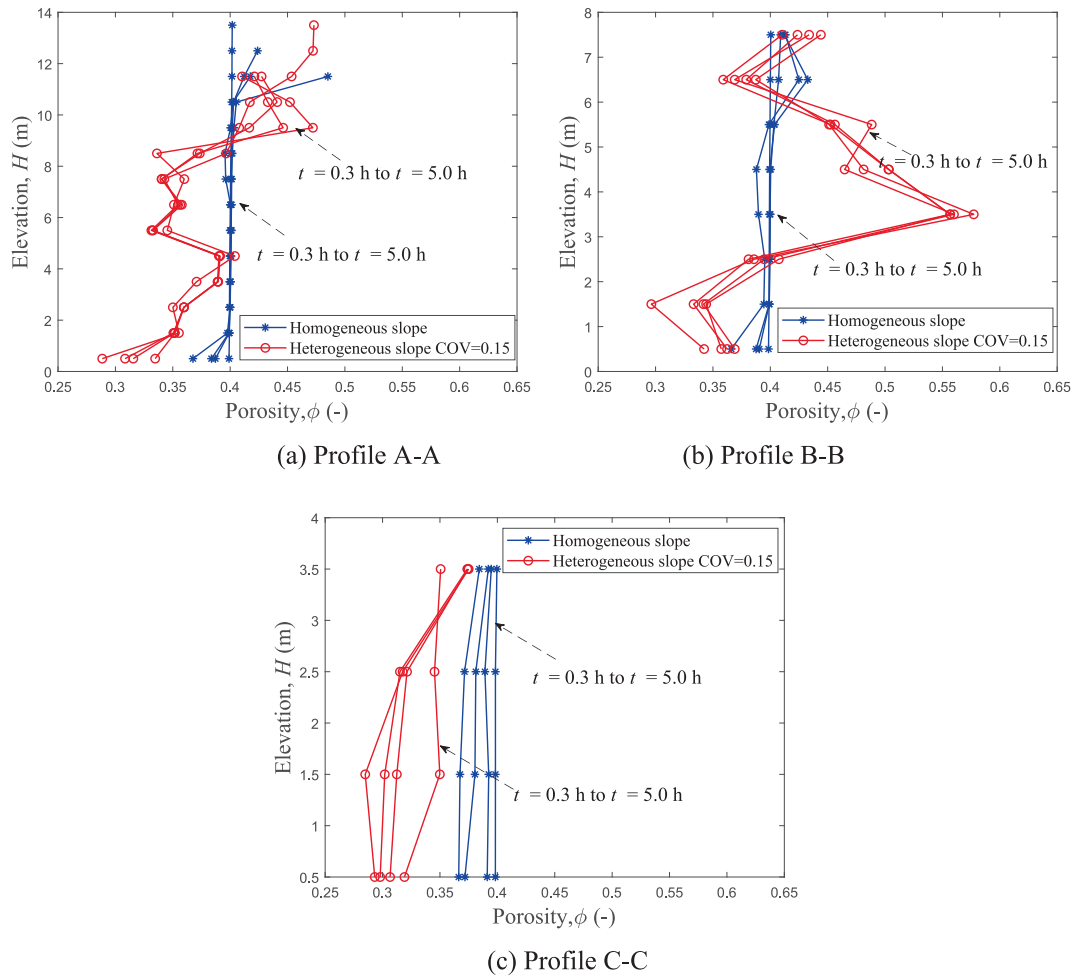


Fig. 15. Evolution of porosity in homogeneous versus heterogeneous slopes.

observed under unsaturated conditions before  $t = 3.3$  h, due to the smaller porosity.

Fig. 17 illustrates the evolution of mean effective stress along profiles A-A, B-B, and C-C. In the homogeneous slope at profile A-A, the mean effective stress is distributed almost linearly with elevation. At  $t = 2.5$  h, the mean effective stress decreases significantly due to the slope collapse. After  $t = 3.3$  h, the infiltration wetting process, without the generation of positive pore water pressure, only slightly reduces the mean effective stress. In the heterogeneous slope, the random distribution of porosity significantly influences soil density, causing fluctuations of the mean effective stress with elevation. Generally, lower porosity indicates denser soil and results in higher mean effective stress, whereas higher porosity corresponds to a looser state and lower mean effective stress. Despite these fluctuations, the overall evolution of mean effective stress in the heterogeneous slope follows the same gradual reduction trend observed in the homogeneous slope.

The evolution of mean effective stress in profile B-B for both homogeneous and heterogeneous slopes shows a similar trend to that in profile A-A. In profile B-B, a notable drop in mean effective stress above the elevation of 3 m is observed in the heterogeneous slope because of a significant increase in porosity at the same elevation. Conversely, a significant increase in mean effective stress in the heterogeneous slope is observed below 3 m, because of the reduction in porosity at the same elevations. In profile C-C, the heterogeneous slope exhibits higher mean effective stress than the homogeneous slope due to lower initial porosity and higher density. These results further demonstrate the dominant influence of porosity on mean effective stress.

Fig. 18 shows the displacement of selected surface locations (points

D, E, and F) for both the homogeneous and heterogeneous slopes. In the homogeneous slope, the wetting-induced collapse occurs at approximately 2.5 h. The displacement at the top (point D) and middle (point E) of the slope reaches up to 5.5 m, while the displacement at point F located near the toe of the slope is about 5 m. In contrast, the wetting-induced collapse occurs half hour earlier in the heterogeneous slope. The displacements of the three points are slightly larger than those in the homogeneous slope, indicating a slightly greater runout distance in the heterogeneous soil slope.

Fig. 19 presents the velocity profiles at points D, E, and F. In the homogeneous slope, the maximum velocity during slope failure reaches up to 1.5 m/s across all locations. In the heterogeneous slope, similar velocity profiles are observed; however, the failure is triggered earlier.

To investigate the spatial variability of void ratio (or porosity) on slope failure, coefficients of variation (COV) of 0.1 and 0.2, and correlation length  $\theta(\phi)$  of 5 m and 7 m were tested. Table 6 summarises the setup of all tested cases and presents the statistics of the mean run-out distance and mean sliding area. According to Table 6, increasing the COV does not significantly affect the mean run-out distance, only a slight increase is observed. This is because the run-out distance is mainly controlled by the critical friction angle of the soil, which remains constant throughout this study. In contrast, the mean sliding area is more sensitive to changes in COV. As the COV increases, the likelihood of deep-seated failure rises, resulting in a larger sliding area. This observation aligns with the findings reported by Fang et al., (2024). As the COV increases, the onset of failure times significantly decreases, reaching approximately 2.0 h. This is because, although increasing the COV increases porosity variability, the impact of porosity on the initial

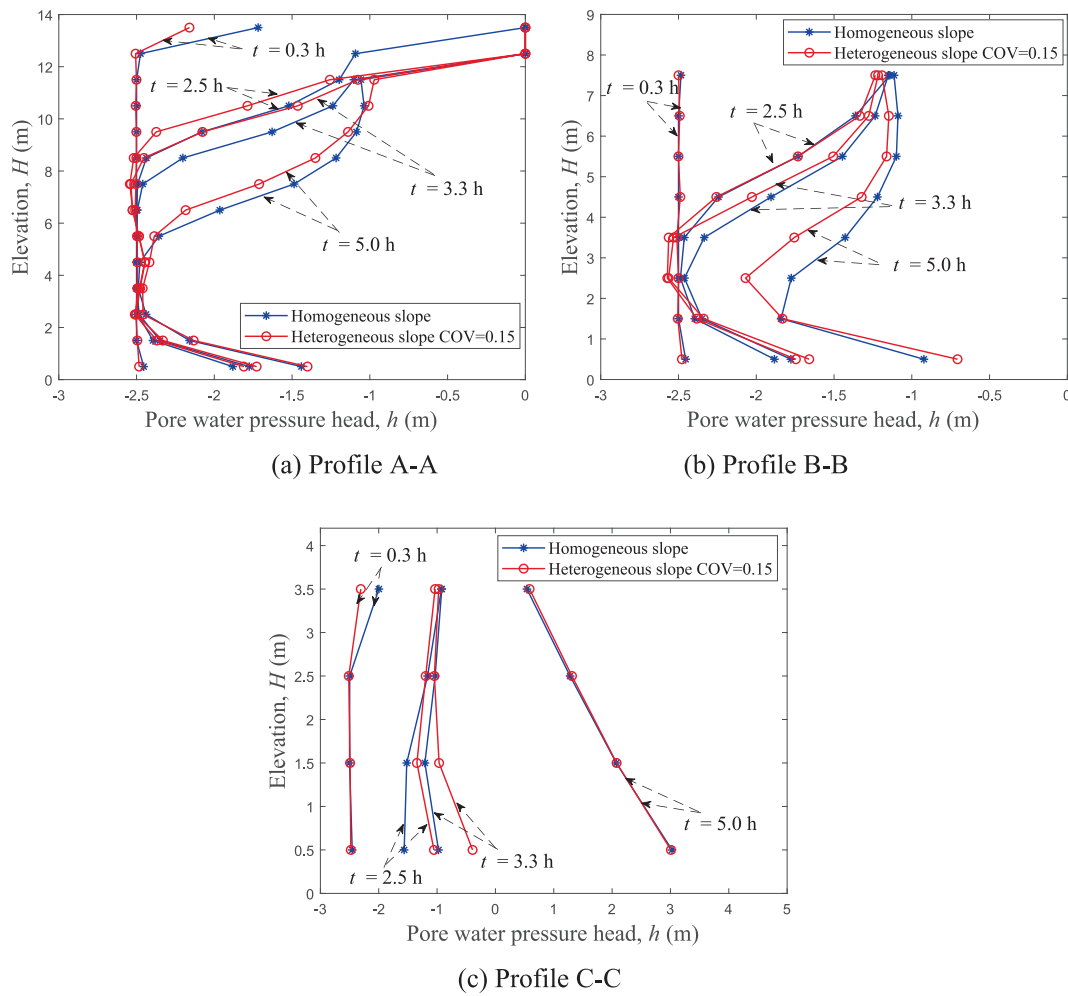


Fig. 16. Evolution of pore water pressure in homogeneous versus heterogeneous slopes.

degree of saturation and the relative permeability coefficient remains small due to the selected SWCC parameter values, as illustrated in Fig. 1. Despite the limited effect of random porosity on the initial hydraulic conditions, it still produced significant differences in the numerical results between the heterogeneous and homogeneous cases. The parameters of the soil water characteristic curve play a more critical role in governing infiltration processes, which in turn have a greater impact on failure time. Similarly, the influence of correlation length on onset time of failure and runout distance is very limited. Increasing the correlation length can slightly enlarge the sliding area. However, this influence becomes negligible when the correlation length exceeds approximately 7 m.

While the cases presented here focus on the influences of spatial variability in porosity, other factors, such as the parameters of the soil water characteristic curve and rainfall intensity also play a significant role in slope failure. This study focuses on the influence of initial porosity heterogeneity on rainfall-induced slope failure using a fully coupled SPH approach. Under identical SWCC parameters, except for the parameter  $g_a$  related to void ratio, increasing porosity variability alters degree of saturation and the permeability coefficient, which promotes preferential seepage, accelerates infiltration, and triggers earlier slope failure. Previous studies (e.g., Zhang et al., 2005, Rahimi et al., 2010) have shown that SWCC fitting parameters strongly influence slope stability. Rahimi et al. (2010) reported in low permeable soil, where the factor of safety varies significantly with the change of SWCC parameters. In contrast, high permeable soils are less sensitive to SWCC variations. However, very few studies have directly applied random field

approaches to model spatial variability in SWCC parameters for rainfall-induced slope failure, due to the numerous variables involved. Many investigations (e.g., Rahimi et al., 2011, Zhang et al., 2011, Kristo et al., 2017) have also demonstrated that more intense rainfall can substantially reduce matric suction, elevate groundwater levels, and significantly lower the factor of safety. Future research will incorporate variable SWCC parameters and rainfall intensities to provide a more comprehensive evaluation.

## 6. Conclusions

This study developed and implemented a fully coupled smoothed particle hydrodynamics (SPH) numerical framework to investigate rainfall-induced unsaturated slope failures, with particular emphasis on the void ratio dependence and variability in unsaturated soils. The advanced unsaturated constitutive model was successfully integrated into the SPH framework to capture the complex hydro-mechanical interactions during slope failure processes. The performance of the unsaturated constitutive model was validated in element level first and then was verified through the SPH simple shear test and granular collapse test.

Application of the fully coupled SPH model to a rainfall infiltration scenario in an unsaturated embankment slope provided critical insights into how spatial heterogeneity in porosity affects water infiltration patterns, pore pressure development, effective stress and slope stability. Increasing the spatial variability of the void ratio generally enhances the potential instability of the slope and creates more preferential paths for

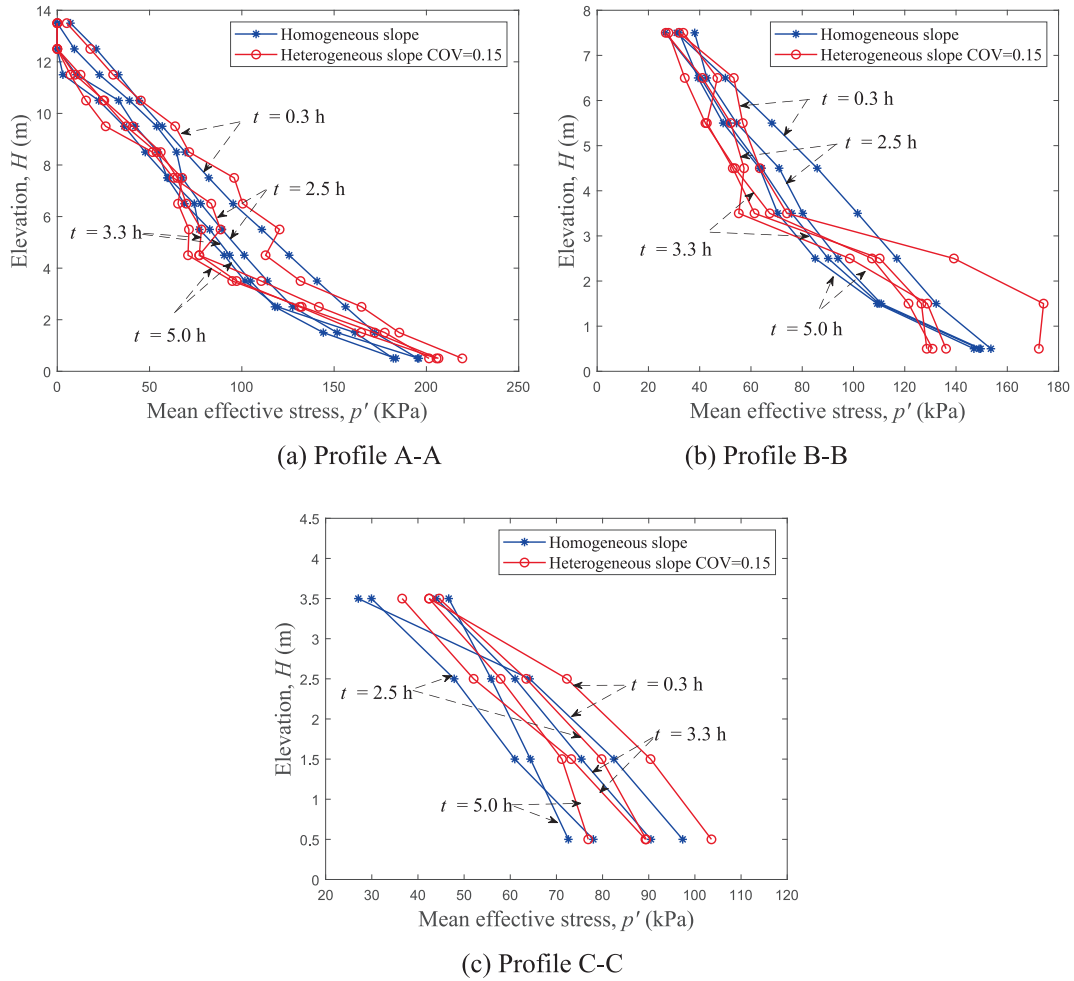


Fig. 17. Evolution of mean effective stress in homogeneous versus heterogeneous slopes.

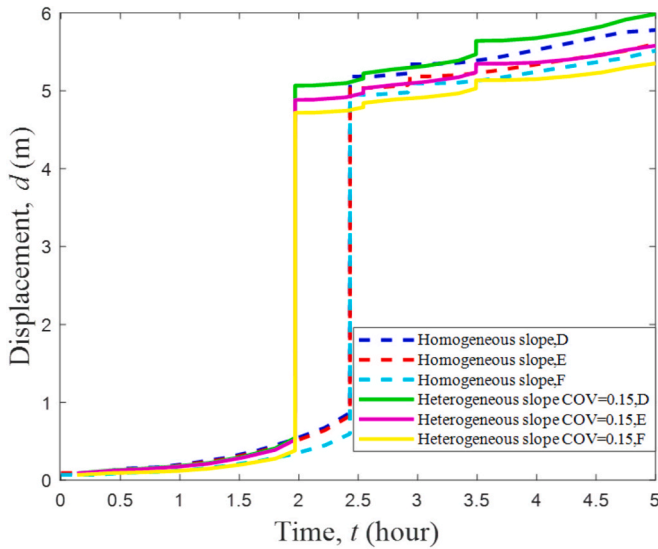


Fig. 18. Displacements at locations of D, E, F in homogeneous and heterogeneous slopes.

seepage flow. As a result, infiltration time is shortened, and the soil's strength deteriorates due to significant variability in density. Numerical results indicate that increasing the spatial variability of the void ratio enlarges the sliding area during slope failure, while it has a limited

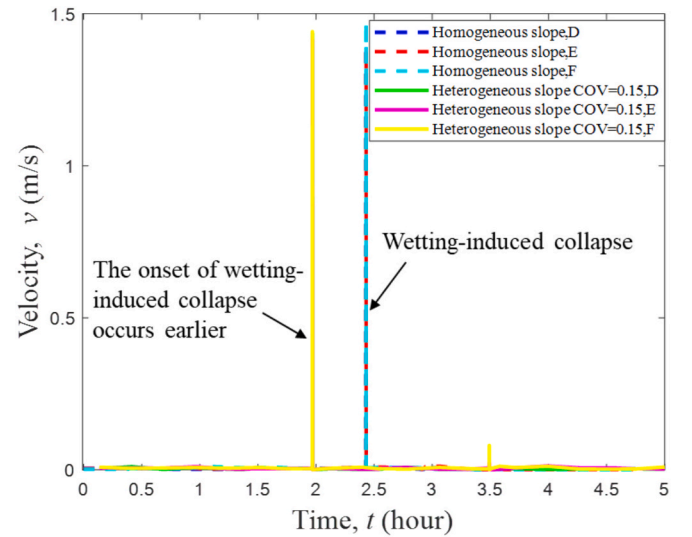


Fig. 19. Velocities at locations of D, E, F in homogeneous and heterogeneous slopes.

impact on the run-out distance. It also leads to an earlier onset of slope failure.

Overall, the proposed SPH-based approach provides a robust and efficient tool for analysing complex slope failure mechanisms in



**Table 6**Influence of COV and  $\theta(\phi)$  of porosity on slope failure.

Cases	Mean porosity ( $\phi$ )	Coefficients of variation (COV)	Correlation length $\theta(\phi)$	Failure onset time	Mean run-out distance	Mean sliding area
0	0.4	0.0	0	2.5 h	4.9 m	27.8 m <sup>2</sup>
1	0.4	0.1	3	2.1 h	4.9 m	28.3 m <sup>2</sup>
2	0.4	0.2	3	2.0 h	5.3 m	33.9 m <sup>2</sup>
3	0.4	0.15	3	2.0 h	5.1 m	29.1 m <sup>2</sup>
4	0.4	0.15	5	2.0 h	5.1 m	31.8 m <sup>2</sup>
5	0.4	0.15	7	2.0 h	5.1 m	32.4 m <sup>2</sup>

unsaturated soils. The findings offer valuable guidance and lay a solid foundation for future probabilistic and performance-based slope stability assessments under rainfall conditions, especially in heterogeneous geomaterials.

#### CRediT authorship contribution statement

**Guodong Ma:** Writing – original draft, Validation, Software, Methodology, Investigation, Formal analysis, Data curation, Conceptualization. **Annan Zhou:** Writing – review & editing, Supervision, Resources, Project administration, Methodology, Funding acquisition, Formal analysis, Conceptualization. **Ha H. Bui:** Writing – review & editing,

Supervision.

#### Declaration of competing interest

The authors declare that they have no known competing financial interests or personal relationships that could have appeared to influence the work reported in this paper.

#### Acknowledgement

Financial support from the Australian Research Council through the Future Fellowship scheme (FT220100515) is gratefully acknowledged.

#### Appendix

The semi-implicit algorithm for the unsaturated constitutive model is presented in Table 7.

**Table 7**

Semi-implicit algorithm for the unsaturated constitutive model.

1	Given strain rate ( $d\epsilon$ ) and other state variables at $t_N$
2	Elastic trial stress increment: $d\sigma_{N+1}^{e\text{ trial}} = \mathbf{D}^e : d\epsilon$ Trial stress: $\sigma_{N+1}^{e\text{ trial}} = \sigma_N^e + d\sigma_{N+1}^{e\text{ trial}}$ Update $p_{N+1}^{e\text{ trial}}, q_{N+1}^{e\text{ trial}}, s_{N+1}, e_{N+1}, s_{eN+1}, s_{eN+1}, \lambda_{N+1}(s_{eN+1})$  Trial internal variables: $p_{0N+1}^{e\text{ trial}} = p_{0N}^{e\text{ trial}}, p_{0N+1}'(s_{eN+1}) = p_c \left( \frac{p_{0N+1}^{e\text{ trial}}}{p_c} \right)^{\frac{\lambda_0 - \kappa}{\lambda_{N+1}(s_{eN+1}) - \kappa}}$
3	Check if plastic yielding occurs by computing $f_{N+1}$ : $f_{N+1}(p_{N+1}^{e\text{ trial}}, q_{N+1}^{e\text{ trial}}, p_{0N+1}', s_{eN+1}) = p_{N+1}^{e\text{ trial}} + \frac{q_{N+1}^{e\text{ trial}2}}{M^2 p_{N+1}^{e\text{ trial}}} - p_{0N+1}'(s_{eN+1})$ If $f_{N+1} < 0$ then Proceed to Step 4 Else $f_{N+1} \geq 0$ , the loading step is elasto-plastic Proceed to Step 5 End
4	Elastic stress update: $\sigma_{N+1}' = \sigma_{N+1}^{e\text{ trial}}, \epsilon_{N+1}^p = \epsilon_N^p$
5	Elasto-plastic step, perform stress corrector: Compute $d\lambda$ : $d\lambda = \frac{f_{N+1}^{e\text{ trial}}}{\frac{\partial f}{\partial \sigma} : \mathbf{D}^e : \frac{\partial g_N}{\partial \sigma} - \frac{\partial f}{\partial p_0} \frac{\partial p_0(s_e)}{\partial p_0} \frac{dp_0}{d\epsilon_v^p} \frac{dg}{dp}}$ Correct the stress and computer other variables: $d\sigma_{N+1}' = \sigma_{N+1}^{e\text{ trial}} - d\sigma^p = \sigma_{N+1}^{e\text{ trial}} - d\lambda \frac{\partial g}{\partial \sigma} \sigma_{N+1}' = \sigma_N^e + d\sigma_{N+1}^{e\text{ trial}}; \text{ Convert to } p_{N+1}' \text{ and } q_{N+1}'$ $\epsilon_{N+1}^p = \epsilon_N^p + d\epsilon_{N+1}^p; e_{N+1} = e_N + de$ $dp_0^e = \frac{(1 + e_{N+1})p_0^e}{(\lambda_0 - \kappa)} \Omega de_v^p; p_{0N+1}' = p_{0N}^e + dp_0^e; p_{0N+1}'(s_{eN+1}) = p_c \left( \frac{p_{0N+1}^e}{p_c} \right)^{\frac{\lambda_0 - \kappa}{\lambda_{N+1}(s_{eN+1}) - \kappa}}$ $dp_0^e = \frac{(1 + e_{N+1})p_0^e}{(\lambda_0 - \kappa)} de_v^p; p_{0N+1}' = p_{0N}^e + dp_0^e; p_{0N+1}'(s_{eN+1}) = p_c \left( \frac{p_{0N+1}^e}{p_c} \right)^{\frac{\lambda_0 - \kappa}{\lambda_{N+1}(s_{eN+1}) - \kappa}}$ $R_{N+1} = \frac{p_{0N+1}'(s_{eN+1})}{p_{0N+1}'(s_{eN+1})}$ EXIT the algorithm

#### Data availability

Data will be made available on request.

#### References

- Alonso, E. E. (2021). Triggering and motion of landslides. *Géotechnique*, 71(1), 3–59.  
Alonso, E.E., Gens, A., Josa, A., 1990. A constitutive model for partially saturated soils. *Géotechnique* 40 (3), 405–430.

- Amarasinghe, M.P., Kulatilaka, S.A.S., Robert, D.J., Zhou, A., Jayathissa, H.A.G., 2024. Risk assessment and management of rainfall-induced landslides in tropical regions: A review. *Nat. Hazards* 120 (3), 2179–2231.
- Andrade, J.E., Baker, J.W., Ellison, K.C., 2008. Random porosity fields and their influence on the stability of granular media. *Int. J. Numer. Anal. Meth. Geomech.* 32 (10), 1147–1172.
- Baum, R.L., Godt, J.W., 2010. Early warning of rainfall-induced shallow landslides and debris flows in the USA. *Landslides* 7 (3), 259–272.
- Bishop, A.W., 1959. The principal of effective stress. *Teknisk ukeblad* 39, 859–863.
- Borja, R.I., White, J.A., 2010. Continuum deformation and stability analyses of a steep hillside slope under rainfall infiltration. *Acta Geotech.* 5 (1), 1–14.
- Bui, H.H., Fukagawa, R., 2013. An improved SPH method for saturated soils and its application to investigate the mechanisms of embankment failure: Case of hydrostatic pore-water pressure. *Int. J. Numer. Anal. Meth. Geomech.* 37 (1), 31–50.
- Bui, H.H., Fukagawa, R., Sako, K., Ohno, S., 2008. Lagrangian meshfree particles method (SPH) for large deformation and failure flows of geomaterial using elastic-plastic soil constitutive model. *Int. J. Numer. Anal. Meth. Geomech.* 32 (12), 1537–1570.
- Bui, H.H., Nguyen, G.D., 2017. A coupled fluid-solid SPH approach to modelling flow through deformable porous media. *Int. J. Solids Struct.* 125, 244–264.
- Bui, H.H., Nguyen, G.D., 2021. Smoothed particle hydrodynamics (SPH) and its applications in geomechanics: From solid fracture to granular behaviour and multiphase flows in porous media. *Comput. Geotech.* 138, 104315.
- Bui, H.H., Sako, K., Fukagawa, R., 2007. Numerical simulation of soil–water interaction using smoothed particle hydrodynamics (SPH) method. *J. Terramech.* 44 (5), 339–346.
- Chen, X., Zhang, L., Zhang, L., Zhou, Y., Ye, G., Guo, N., 2021. Modelling rainfall-induced landslides from initiation of instability to post-failure. *Comput. Geotech.* 129, 103877.
- Chiu, C., Yan, W., Yuen, K.-V., 2012. Reliability analysis of soil–water characteristics curve and its application to slope stability analysis. *Eng. Geol.* 135, 83–91.
- Cho, S.E., 2010. Probabilistic assessment of slope stability that considers the spatial variability of soil properties. *J. Geotech. Geoenviron. Eng.* 136 (7), 975–984.
- Dyson, A.P., Tolooiyan, A., 2019. Prediction and classification for finite element slope stability analysis by random field comparison. *Comput. Geotech.* 109, 117–129.
- Fang, H., Li, D., Wang, S., Qu, C., 2024. Hypoplastic modeling post-failure behavior of sandy slope with porosity spatial variability. *Comput. Geotech.* 173, 106470.
- Feng, K., Huang, D., Wang, G., 2021. Two-layer material point method for modeling soil–water interaction in unsaturated soils and rainfall-induced slope failure. *Acta Geotech.* 16 (8), 2529–2551.
- Fenton, G.A., Griffiths, D.V., 2007. Random field generation and the local average subdivision method. In: *Probabilistic methods in geotechnical engineering*. Springer Vienna, Vienna, pp. 201–223.
- Fenton, G.A., Vanmarcke, E.H., 1990. Simulation of random fields via local average subdivision. *J. Eng. Mech.* 116 (8), 1733–1749.
- Galavi, V. (2010). *Groundwater flow, fully coupled flow deformation and undrained analyses in PLAXIS 2D and 3D*. Plaxis report.
- Gallipoli, D., Wheeler, S.J., Karstunen, M., 2003. Modelling the variation of degree of saturation in a deformable unsaturated soil. *Géotechnique* 53 (1), 105–112.
- Griffiths, D., Fenton, G.A., 1993. Seepage beneath water retaining structures founded on spatially random soil. *Géotechnique* 43 (4), 577–587.
- Griffiths, D., Fenton, G.A., 2004. Probabilistic slope stability analysis by finite elements. *J. Geotech. Geoenviron. Eng.* 130 (5), 507–518.
- Griffiths, D., Huang, J., Fenton, G.A., 2009. Influence of spatial variability on slope reliability using 2-D random fields. *J. Geotech. Geoenviron. Eng.* 135 (10), 1367–1378.
- Gingold, R.A., Monaghan, J.J., 1977. Smoothed particle hydrodynamics: theory and application to non-spherical stars. *MNRAS* 181 (3), 375–389.
- Jin, Y.F., Yin, Z.Y., 2022. Two-phase PFEM with stable nodal integration for large deformation hydromechanical coupled geotechnical problems. *Comput. Methods Appl. Mech. Eng.* 392, 114660.
- Kozeny, J., 1927. Ueber kapillare leitung des wassers im boden. *Sitzungsberichte der Akademie der Wissenschaften in Wien* 136, 271.
- Le, T.M.H., Gallipoli, D., Sanchez, M., Wheeler, S., 2013. Rainfall-induced differential settlements of foundations on heterogeneous unsaturated soils. *Géotechnique* 63 (15), 1346–1355.
- Le, T.M.H., Gallipoli, D., Sánchez, M., Wheeler, S., 2015. Stability and failure mass of unsaturated heterogeneous slopes. *Can. Geotech. J.* 52 (11), 1747–1761.
- Le, T.M.H., Gallipoli, D., Sanchez, M., Wheeler, S.J., 2012. Stochastic analysis of unsaturated seepage through randomly heterogeneous earth embankments. *Int. J. Numer. Anal. Meth. Geomech.* 36 (8), 1056–1076.
- Le, T.M.H., Sanchez, M., Gallipoli, D., Wheeler, S., 2019. Probabilistic study of rainfall-triggered instabilities in randomly heterogeneous unsaturated finite slopes. *Transp. Porous Media* 126 (1), 199–222.
- Lian, Y., Bui, H.H., Nguyen, G.D., Haque, A., 2023. An effective and stabilised (u–p) SPH framework for large deformation and failure analysis of saturated porous media. *Comput. Methods Appl. Mech. Eng.* 408, 115967.
- Lian, Y., Bui, H.H., Nguyen, G.D., Tran, H.T., Haque, A., 2021. A general SPH framework for transient seepage flows through unsaturated porous media considering anisotropic diffusion. *Comput. Methods Appl. Mech. Eng.* 387, 114169.
- Lian, Y., Bui, H.H., Nguyen, G.D., Zhao, S., Haque, A., 2022. A computationally efficient SPH framework for unsaturated soils and its application to predicting the entire rainfall-induced slope failure process. *Géotechnique* 74 (8), 787–805.
- Liu, L.-L., Cheng, Y.-M., Zhang, S.-H., 2017. Conditional random field reliability analysis of a cohesion-frictional slope. *Comput. Geotech.* 82, 173–186.
- Liu, X., Wang, Y., 2021. Probabilistic simulation of entire process of rainfall-induced landslides using random finite element and material point methods with hydro-mechanical coupling. *Comput. Geotech.* 132, 103989.
- Lu, M., Ceccato, F., Zhou, M., Yerro, A., Zhang, J., 2024. Evaluating the exceedance probability of the runout distance of rainfall-induced landslides using a two-stage FEM-MPM approach. *Acta Geotech.* 19 (6), 3691–3706.
- Lu, M., Zhang, J., Zhang, L., Zhang, L., 2020. Assessing the annual risk of vehicles being hit by a rainfall-induced landslide: a case study on Kennedy Road in Wan Chai, Hong Kong. *Nat. Hazards Earth Syst. Sci.* 20 (6), 1833–1846.
- Ma, G., Bui, H.H., Lian, Y., Nguyen, T.V., Nguyen, G.D., 2024. Prediction of backward erosion, pipe formation and induced failure using a multi-physics SPH computational framework. *Int. J. Numer. Anal. Meth. Geomech.* 48 (18), 4307–4326.
- Ma, G., Bui, H.H., Lian, Y., Tran, K.M., Nguyen, G.D., 2022. A five-phase approach, SPH framework and applications for predictions of seepage-induced internal erosion and failure in unsaturated/saturated porous media. *Comput. Methods Appl. Mech. Eng.* 401, 115614.
- Masoudian, M.S., Afrapoli, M.A.H., Tasalloti, A., Marshall, A.M., 2019. A general framework for coupled hydro-mechanical modelling of rainfall-induced instability in unsaturated slopes with multivariate random fields. *Comput. Geotech.* 115, 103162.
- Morikawa, D.S., Asai, M., 2022a. A phase-change approach to landslide simulations: Coupling finite strain elastoplastic TLSPH with non-Newtonian IISPH. *Comput. Geotech.* 148, 104815.
- Morikawa, D.S., Asai, M., 2022b. Soil-water strong coupled ISPH based on u–w–p formulation for large deformation problems. *Comput. Geotech.* 142, 104570.
- Mukhlisin, M., Kosugi, K.I., Satofuka, Y., Mizuyama, T., 2006. Effects of soil porosity on slope stability and debris flow runout at a weathered granitic hillslope. *Vadose Zone J.* 5 (1), 283–295.
- Ng, C.W., Qu, C., Ni, J., Guo, H., 2022. Three-dimensional reliability analysis of unsaturated soil slope considering permeability rotated anisotropy random fields. *Comput. Geotech.* 151, 104944.
- Nguyen, C.T., Nguyen, C.T., Bui, H.H., Nguyen, G.D., Fukagawa, R., 2017. A new SPH-based approach to simulation of granular flows using viscous damping and stress regularisation. *Landslides* 14 (1), 69–81.
- Nguyen, D.T., Bui, H.H., Lian, Y., Nguyen, T.T., Nguyen, G.D., Bouazza, A., 2025. A CASM-X constitutive model for unsaturated soils and its application to model wetting-induced slope collapse using SPH. *Comput. Geotech.* 186, 107353.
- Nonoyama, H., Moriguchi, S., Sawada, K., Yashima, A., 2015. Slope stability analysis using smoothed particle hydrodynamics (SPH) method. *Soils Found.* 55 (2), 458–470.
- Ozturk, U., Bozzolan, E., Holcombe, E.A., Shukla, R., Pianosi, F., Wagener, T., 2022. How climate change and unplanned urban sprawl bring more landslides. *Nature* 608 (7922), 262–265.
- Pastor, M., Haddad, B., Sorbino, G., Cuomo, S., Drempetic, V., 2009. A depth-integrated, coupled SPH model for flow-like landslides and related phenomena. *Int. J. Numer. Anal. Meth. Geomech.* 33 (2), 143–172.
- Peng, C., Xu, G., Wu, W., Yu, H.S., Wang, C., 2017. Multiphase SPH modeling of free surface flow in porous media with variable porosity. *Comput. Geotech.* 81, 239–248.
- Phoon, K.-K., Santos, A., Quek, S.-T., 2010. Probabilistic analysis of soil-water characteristic curves. *J. Geotech. Geoenviron. Eng.* 136 (3), 445–455.
- Rahimi, A., Rahardjo, H., Leong, E.C., 2010. Effect of hydraulic properties of soil on rainfall-induced slope failure. *Eng. Geol.* 114 (3–4), 135–143.
- Rahimi, A., Rahardjo, H., Leong, E.C., 2011. Effect of antecedent rainfall patterns on rainfall-induced slope failure. *J. Geotech. Geoenviron. Eng.* 137 (5), 483–491.
- Robbins, B., Griffiths, D., Fenton, G.A., 2021. Random finite element analysis of backward erosion piping. *Comput. Geotech.* 138, 104322.
- Roscoe, K.H., Schofield, A., Thurairajah, A., 1963. Yielding of clays in states wetter than critical. *Géotechnique* 13 (3), 211–240.
- Schofield, A.N., Wroth, C.P., 1968. *Critical State Soil Mechanics*. McGraw-Hill, London.
- Shao, S., 2010. Incompressible SPH flow model for wave interactions with porous media. *Coast. Eng.* 57 (3), 304–316.
- Sheng, D., Sloan, S. W., Gens, A., & Smith, D. W. (2003). Finite element formulation and algorithms for unsaturated soils. Part I: Theory. *International journal for numerical and analytical methods in geomechanics*, 27(9), 745-765.
- Showkat, R., Mohammadi, H., Babu, G.S., 2022. Effect of rainfall infiltration on the stability of compacted embankments. *Int. J. Geomech.* 22 (7), 04022104.
- Solowski, W., Sloan, S., 2015. Evaluation of material point method for use in geotechnics. *Int. J. Numer. Anal. Meth. Geomech.* 39 (7), 685–701.
- Sun, D.A., Sheng, D., Xu, Y., 2007. Collapse behaviour of unsaturated compacted soil with different initial densities. *Can. Geotech. J.* 44 (6), 673–686.
- Tohari, A., Nishigaki, M., Komatsu, M., 2007. Laboratory rainfall-induced slope failure with moisture content measurement. *J. Geotech. Geoenviron. Eng.* 133 (5), 575–587.
- Uzielli, M., Lacasse, S., Nadim, F., Phoon, K., 2007. Soil variability analysis for geotechnical practice. Characterisation and engineering properties of natural soils 3 (4), 1653–1752.
- Van Genuchten, M.T., 1980. A closed-form equation for predicting the hydraulic conductivity of unsaturated soils. *Soil Sci. Soc. Am. J.* 44 (5), 892–898.
- Vignjevic, R., Djordjevic, N., Gemkow, S., De Vuyst, T., Campbell, J., 2014. SPH as a nonlocal regularisation method: Solution for instabilities due to strain-softening. *Comput. Methods Appl. Mech. Eng.* 277, 281–304.
- Wang, L., Tang, L., Wang, Z., Liu, H., Zhang, W., 2020. Probabilistic characterization of the soil-water retention curve and hydraulic conductivity and its application to slope reliability analysis. *Comput. Geotech.* 121, 103460.

- Wang, S., Fang, H.J., Kang, X., Li, D.Q., Wu, W., 2024. Simhypo-sand: a simple hypoplastic model for granular materials and SPH implementation. *Acta Geotech.* 19 (7), 4533–4555.
- Wei, X., Zhang, L., Yang, H.-Q., Zhang, L., Yao, Y.-P., 2021. Machine learning for pore-water pressure time-series prediction: Application of recurrent neural networks. *Geosci. Front.* 12 (1), 453–467.
- Wheeler, S.J., Sivakumar, V., 1995. An elasto-plastic critical state framework for unsaturated soil. *Géotechnique* 45 (1), 35–53.
- Xiong, W., Jiang, S.-H., Wan, J.-H., Zhou, C.-B., Gao, L., 2025. Probabilistic investigation of the whole process of backward erosion piping for a two-layered levee in spatially variable soils. *Comput. Geotech.* 184, 107244.
- Xue, Y., Chen, N., Tang, R., Yang, Z., Jiao, M., Wen, T., Jin, J., 2025. Slope failure mechanism of the “5·1” Meida Highway collapse in Guangdong, China: interaction between multi-source water and weathered granite soil. *Landslides* 22 (4), 1199–1212.
- Yang, H.Q., Zhang, L., 2024. Bayesian back analysis of unsaturated hydraulic parameters for rainfall-induced slope failure: A review. *Earth Sci. Rev.* 251, 104714.
- Yang, H.Q., Zhang, L., Gao, L., Phoon, K.K., Wei, X., 2022. On the importance of landslide management: Insights from a 32-year database of landslide consequences and rainfall in Hong Kong. *Eng. Geol.* 299, 106578.
- Yao, Y.P., Hou, W., Zhou, A.N., 2009. UH model: three-dimensional unified hardening model for overconsolidated clays. *Géotechnique* 59 (5), 451–469.
- Yao, Y.P., Gao, Z., Zhao, J., Wan, Z., 2012. Modified UH model: constitutive modeling of overconsolidated clays based on a parabolic Hvorslev envelope. *J. Geotech. Geoenviron. Eng.* 138 (7), 860–868.
- Yerro, A., Alonso, E.E., Pinyol, N.M., 2015. The material point method for unsaturated soils. *Géotechnique* 65 (3), 201–217.
- Yu, H.-S., 1998. CASM: A unified state parameter model for clay and sand. *Int. J. Numer. Anal. Meth. Geomech.* 22 (8), 621–653.
- Yuan, W.-H., Wang, B., Zhang, W., Jiang, Q., Feng, X.-T., 2019. Development of an explicit smoothed particle finite element method for geotechnical applications. *Comput. Geotech.* 106, 42–51.
- Yuan, W.H., Zhu, J.X., Liu, K., Zhang, W., Dai, B.B., Wang, Y., 2022. Dynamic analysis of large deformation problems in saturated porous media by smoothed particle finite element method. *Comput. Methods Appl. Mech. Eng.* 392, 114724.
- Yubonchit, S., Chinkulkijniwat, A., Horpibulsuk, S., Jothityangkoon, C., Arulrajah, A., Suddeepong, A., 2017. Influence factors involving rainfall-induced shallow slope failure: numerical study. *Int. J. Geomech.* 17 (7), 04016158.
- Zhang, L.L., Zhang, L.M., Tang, W.H., 2005. Rainfall-induced slope failure considering variability of soil properties. *Geotechnique* 55 (2), 183–188.
- Zhang, Y., Zhou, A.N., Nazem, M., Carter, J., 2019. Finite element implementation of a fully coupled hydro-mechanical model and unsaturated soil analysis under hydraulic and mechanical loads. *Comput. Geotech.* 110, 222–241.
- Zhang, W., Zhong, Z.-H., Peng, C., Yuan, W.-H., Wu, W., 2021. GPU-accelerated smoothed particle finite element method for large deformation analysis in geomechanics. *Comput. Geotech.* 129, 103856.
- Zhou, A.N., Sheng, D., Sloan, S.W., Gens, A., 2012a. Interpretation of unsaturated soil behaviour in the stress-saturation space, I: volume change and water retention behaviour. *Comput. Geotech.* 43, 178–187.
- Zhou, A.N., Sheng, D., Sloan, S.W., Gens, A., 2012b. Interpretation of unsaturated soil behaviour in the stress-saturation space: II: constitutive relationships and validations. *Comput. Geotech.* 43, 111–123.
- Zhou, A.N., Sheng, D., 2015. An advanced hydro-mechanical constitutive model for unsaturated soils with different initial densities. *Comput. Geotech.* 63, 46–66.
- Zhu, C., Wu, W., Peng, C., Wang, S., Wei, X., 2024. SPH implementation of a critical state-based hypoplastic model for granular materials in large-deformation problems. *Comput. Geotech.* 166, 106011.